Petroleum Science 21 (2024) 4278–4297

Contents lists available at ScienceDirect

Petroleum Science

journal homepage: www.keaipublishing.com/en/journals/petroleum-science

Original Paper

Interwell interference model of horizontal wells in shale gas reservoirs based on multi-connected boundary element method

Yu-Long Zhao [a, *], Hao-Yan Feng [a], Cheng-Zhong Bu [b], Li-Sha Zhou [c], Jian-Fa Wu [c], Lie-Hui Zhang [a], Ying-Fang Zhou [d]

[a] State Key Laboratory of Oil and Gas Reservoir Geology and Exploitation, Chengdu, 610500, Sichuan, PR China
[b] Shale Gas Exploration and Development Project Management Department of CNPC Chuanqing Drilling Engineering Company Limited, Chengdu, 610051, Sichuan, PR China
[c] PetroChina Southwest Oil & Gas Field Company, Chengdu, 610051, Sichuan, PR China
[d] University of Aberdeen, School of Engineering, King's College, Aberdeen, AB24 3UE, Scotland, UK

ARTICLE INFO

Article history:
Received 13 May 2024
Received in revised form
27 August 2024
Accepted 27 August 2024
Available online 29 August 2024

Edited by Yan-Hua Sun

Keywords:
Interwell interference
Multi-connected boundary element method
Shale gas reservoirs
Complex flow mechanisms
Transient analysis

ABSTRACT

Due to the wide application of closely spaced multi-well horizontal pads for developing unconventional gas reservoirs, interference between wells becomes a significant concern. Communication between wells mainly occurs through natural fractures. However, previous studies have found that interwell communication through natural fractures is varied, and non-communication also appears in the mid and late stages of production due to natural fracture closure. This study proposes a boundary element method for coupling multi-connected regions for the first time. Using this method, we coupled multiple flow fields to establish dual-well models with various connectivity conditions of the stimulated reservoir volume (SRV) region. These models also take into consideration of adsorption and desorption mechanism of natural gas as well as the impact of fracturing fluid retention.

The study found that when considering the non-communication of SRV regions between multi-well horizontal pads, the transient behavior of the targeted well exhibits a transitional flow stage occurring before the well interference flow stage. In addition, sensitivity analysis shows that the well spacing and production regime, as well as the connectivity conditions of the SRV region, affect the timing of interwell interference. Meanwhile, the productivity of the two wells, reservoir properties, and fracturing operations affect the intensity of interwell interference.

1. Introduction

As unconventional oil and gas reservoirs are mostly characterized by low porosity and low permeability, multi-fractured horizontal wells (MFHWs) have become the most effective means of extracting for shale gas reservoirs (Asadi et al., 2020; Cui et al., 2021; He et al., 2018; Guo et al., 2016; Mayerhofer et al., 2010; Wang et al., 2022; Zhang et al., 2020). While "small well spacing and dense well network" is the mainstream method of developing shale gas reservoirs, the deployment of excessively small well spacing may lead to serious well interference (Al-Shami et al., 2023; Raterman et al., 2020; Wang et al., 2018). Microseismic events indicate that well interference can be classified into three scenarios: hydraulic fracture communication (fracture hits), nature-fracture communication, and non-communication (Fig. 1). As fracture hits between wells can significantly affect production dynamics and reduce productivity (He et al., 2023; Hou et al., 2022; Li, 2022), it is necessary to scientifically plan well spacing to avoid direct fracture hits. Furthermore, when establishing a multi-well horizontal pad model for systematic evaluation of well interference and optimizing well network density, it is essential to differentiate between two scenarios of nature-fracture communication and non-communication between wells.

Compared to conventional reservoirs, shale gas reservoirs exhibit a more complex pore structure, which contains organic matter pores, inorganic matter pores, and natural fractures (Afsharpoor and Javadpour, 2018; Fu et al., 2021; Han et al., 2019). Varied seepage mechanisms need to be considered for different

* Corresponding author.
E-mail address: 373104686@qq.com (Y.-L. Zhao).

https://doi.org/10.1016/j.petsci.2024.08.009

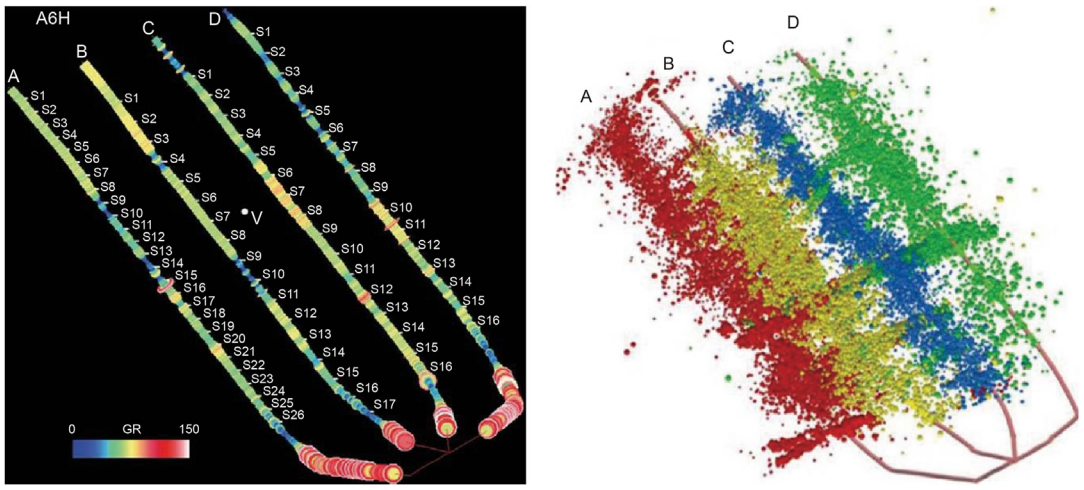

Fig. 1. Microseismic events of the multi-well horizontal pads (Manchanda et al., 2014).

types of pores. The natural gas stored in the pores of organic matter is mainly free gas and adsorbed gas, and the seepage mechanisms include adsorption, desorption, and diffusion of the gas (Zhang et al., 2019; Zhao et al., 2014, 2018). The natural gas stored in the inorganic pore space is only free gas, therefore the flow of gas in such space is relatively simple, only needing to consider the bulk phase flow characteristics. However, experiments and numerical simulations have shown that reservoir-bound water exists as water films or water bridges on the surface or throat of the inorganic matter pore, which impedes the flow of gases and leads to a reduction in the transport capacity of the shale matrix (Li et al., 2018; Tan et al., 2021). Therefore, the effect of bound water saturation needs to be taken into account when establishing the apparent permeability of inorganic matter pores.

In the development of shale gas, the stimulated reservoir volume (SRV) zones created by horizontal well fracture modification can significantly improve subsurface seepage conditions for natural gas to increase horizontal well production. Some scholars have used linear flow modeling to study the transient pressure response and production capacity of fractured horizontal wells in shale gas reservoirs (Garcez and Ayala, 2022; Zhang D.L. et al., 2015; Zhang L.H. et al., 2016). However, such models assume an ideal situation where each hydraulic fracture is parallel, isometric, and homogeneous, which is quite different from the actual situation. Based on this, some researchers derived and established a composite boundary element model, and applied this method to the modeling of fractured horizontal wells, while taking into account the effects of SRV zones and irregular boundaries (Chen and Liu, 2023; Jia et al., 2017b; Wu et al., 2018, 2020).

In recent years, many densely spaced MFHWs have been employed in unconventional reservoirs. However, during large-scale hydraulic fracturing operations, excessive fracture extension can lead to severe well interference. Therefore, the conventional approach of considering individual fractured horizontal well models is no longer applicable. To address this issue, some researchers have conducted studies of the pressure transient behavior of multi-well horizontal pads by establishing numerical models (Siddiqui and Kumar, 2016; Xu et al., 2023; Fu et al., 2023; Marongiu-Porcu et al., 2016). Gao et al. (2019) employed the perpendicular bisection (PEBI) grids and the finite volume method to analyze the pressure transient behavior of MFHWs in shale gas reservoirs under three scenarios: direct hydraulic fracture communication between horizontal wells, communication with SRV regions, and non-communication. Qin et al. (2023) coupled the embedded discrete fracture model with the reservoir model to study the pressure transient behavior of the multi-well horizontal pad with complex fracture networks and analyzed the flow stages of multi-well systems under well interference. Chen et al. (2023) investigated the pressure transient behavior of two-phase flow in multi-well horizontal pads using the perpendicular bisection grids and discrete fracture model. They also conducted a thorough analysis of the effects of various parameters of the targeted well and offsetting well on the well interference flow. Liang et al. (2024) categorized the interference forms into four types and established numerical models. Based on multiple seepage mechanisms in shale gas reservoirs, they investigated the dynamic variation of production between the targeted well and the offsetting well under different interference forms of multi-well horizontal pads in shale gas reservoirs. The well interference investigations conducted through numerical methods offer comprehensive insights into the impact of offsetting wells on targeted wells under various scenarios. Furthermore, they conducted sensitivity analyses on pertinent parameters, thereby significantly enhancing the understanding and value of the research in this field.

However, due to the requirement of subdividing a large number of grids to ensure computational accuracy, numerical models are inevitably inefficient and demand high computational power. Therefore, establishing a parametric or semi-parametric model is necessary for analyzing the transient behavior of multi-well horizontal pads. Molina and Zeidouni (2017a, 2017b) developed an analytical model for MFHWs that considers interwell interference based on linear flow theory. Using this model, they analyzed various dual-MFHWs systems and used the interference coefficient α as a fitting parameter to perform history matching. Their study found a strong correlation between the interference coefficient α and the degree of interwell pressure communication. Two years later, Molina (2019) extended this method to the three-MFHWs system and applied the analytical model to evaluate the degree of fracture hits in actual multi-well horizontal pads. However, the multi-well platform model based on linear flow theory makes overly idealized assumptions about fracture geometry and flow regions. While this method allows for quick processing of field data, it also introduces certain errors.

Some scholars have studied the pressure transient behavior of multi-well horizontal pads by establishing semi-analytical models based on source functions (Jia et al., 2017a; Guo et al., 2023). These models are capable of characterizing the complex fractures in fractured horizontal wells and have been widely applied. However,

they demonstrate the limitation of only considering regular flow boundaries, thus being unable to accurately describe the complex SRV regions generated by the fracturing operation. The boundary element method, as a semi-analytical approach developed based on the source functions, addresses the challenges of complex boundaries, offering advantages such as no need for grid partitioning, fast computation, and high accuracy. Chu et al. (2022a, 2022b) employed the boundary element method to analyze the effects of offsetting well and boundaries, as well as the pressure transient behavior of multi-well horizontal pads from both three-dimensional and two-dimensional perspectives. In the same year, they further utilized this method to establish a model to analyze the SRV region and conducted a detailed analysis of the impact of SRV region shape on pressure transient behavior. However, the aforementioned semi-analytical models did not distinguish between communication and non-communication with SRV regions among multi-well horizontal pads. Instead, they represented the SRV region as a unified entity. According to Kumar et al. (2020), many wells exhibit direct fracture connectivity in the early stages. However, during the production process, the connected fracture pathways will close. Therefore, for different types and periods of well interference, more detailed models of various types are required.

This study divides the interwell interference of multi-well horizontal pad into three scenarios: fully connected with SRV regions, partially connected with SRV regions, and non-communication (Fig. 2), and proposes and applies for the first time the multi-connected boundary element method to establish a coupled model of multiple flow fields, and the Green's functions, point source functions, and perturbation transformations were combined to solve the model. We compared the interwell interference of multi-well horizontal pads under different scenarios and analyzed the impact of well spacing, SRV properties, and offsetting well parameters on the pressure behavior of targeted wells. The research findings aim to provide new solutions for the spacing arrangement of MFHWs in shale gas reservoirs.

2. Gas transporting mechanisms

The seepage mechanism of gas in shale is complex, and residual fracturing fluids often occur in the SRV area around the horizontal wells after the fracturing operation is finished, which makes the gas flow in shale more complicated. The model in this study not only considers the adsorption and desorption behavior of gas in organic pores but also takes into account the effect of fracturing fluid (bound water) trapped in inorganic pores on gas seepage.

2.1. Apparent permeability of organic pores

2.1.1. Viscous flow

In a shale matrix, the flow of gas can be expressed by the Darcy equation:

$$v = -\frac{k}{\mu_g}\nabla p \tag{1}$$

where v is the velocity, m/s; k is the permeability, m^2; μ_g is the viscosity of shale gas, Pa·s; and p is the pressure of pores, Pa, ∇ is the Hamilton operator.

For gases, the mass flux due to viscous flow can be described as

$$J_v = -\frac{pM_g}{ZRT}\frac{k}{\mu_g}\nabla p \tag{2}$$

where J_v is the mass flux due to viscous flow, kg/(m^2·s); M_g is the molar mass, kg/mol; Z is a dimensionless deviation factor; R is the gas constant, J/(mol·K); T is the temperature of the reservoir, K.

2.1.2. Knudsen diffusion

The mass flux of shale gas due to Knudsen diffusion is expressed as follows:

$$J_k = -\frac{D_k p M_g c_g}{ZRT}\nabla p \tag{3}$$

where J_k is the mass flux due to Knudsen diffusion, kg/(m^2·s); D_k is the Knudsen diffusion coefficient, m^2/s; c_g is the gas compressibility factor, Pa^{-1}.

The total mass flow considering viscous flow with Knudsen diffusion is expressed as

$$J = J_v + J_k = -\frac{\rho_g}{\mu_g}\left(k_m + D_k\mu_g c_g\right)\nabla p \tag{4}$$

The equivalent apparent permeability of organic pores can be expressed as

$$k_{app\text{-}or} = k_m + D_k\mu_g c_g \tag{5}$$

where ρ_g is the gas density, kg/mol; $k_{app\text{-}or}$ is the apparent permeability of organic pores, m^2; k_m is the matrix permeability, m^2.

Considering the gas slippage, Eq. (5) can be rewritten as

$$k_{app\text{-}or} = Fk_m + D_k\mu_g c_g \tag{6}$$

$$F = 1 + \frac{\mu_g}{31.623 p_{avg}}\sqrt{\frac{\pi RT\phi}{\tau M_g k_m}} \tag{7}$$

where F is the slippage coefficient, dimensionless; τ is the tortuosity of the pore; ϕ is the porosity of the matrix; p_{avg} is the average pressure in pores, Pa.

2.1.3. Langmuir isothermal adsorption equation

According to previous studies (Zhao et al., 2016), free gas and adsorbed gas are always in dynamic equilibrium during the development of shale gas reservoirs, which can be described by the Langmuir equation:

$$G = G_L\frac{p}{p_L + p} \tag{8}$$

where G is the adsorption quantity of gas, m^3/m^3; G_L is the limiting adsorption quantity of gas, m^3/m^3; p_L is the Langmuir pressure, Pa.

2.2. Apparent permeability of inorganic pores

Considering the effects of the bound water, the permeability of the porous medium is

$$k_w = \frac{\phi(r - h_w)^2}{8\tau} \tag{9}$$

where k_w is the permeability under consideration of the effect of the bound water, m^2; h_w is the bound water film thickness, m; r is the pore radius, m.

The bound water film thickness is related to the reservoir-bound water saturation:

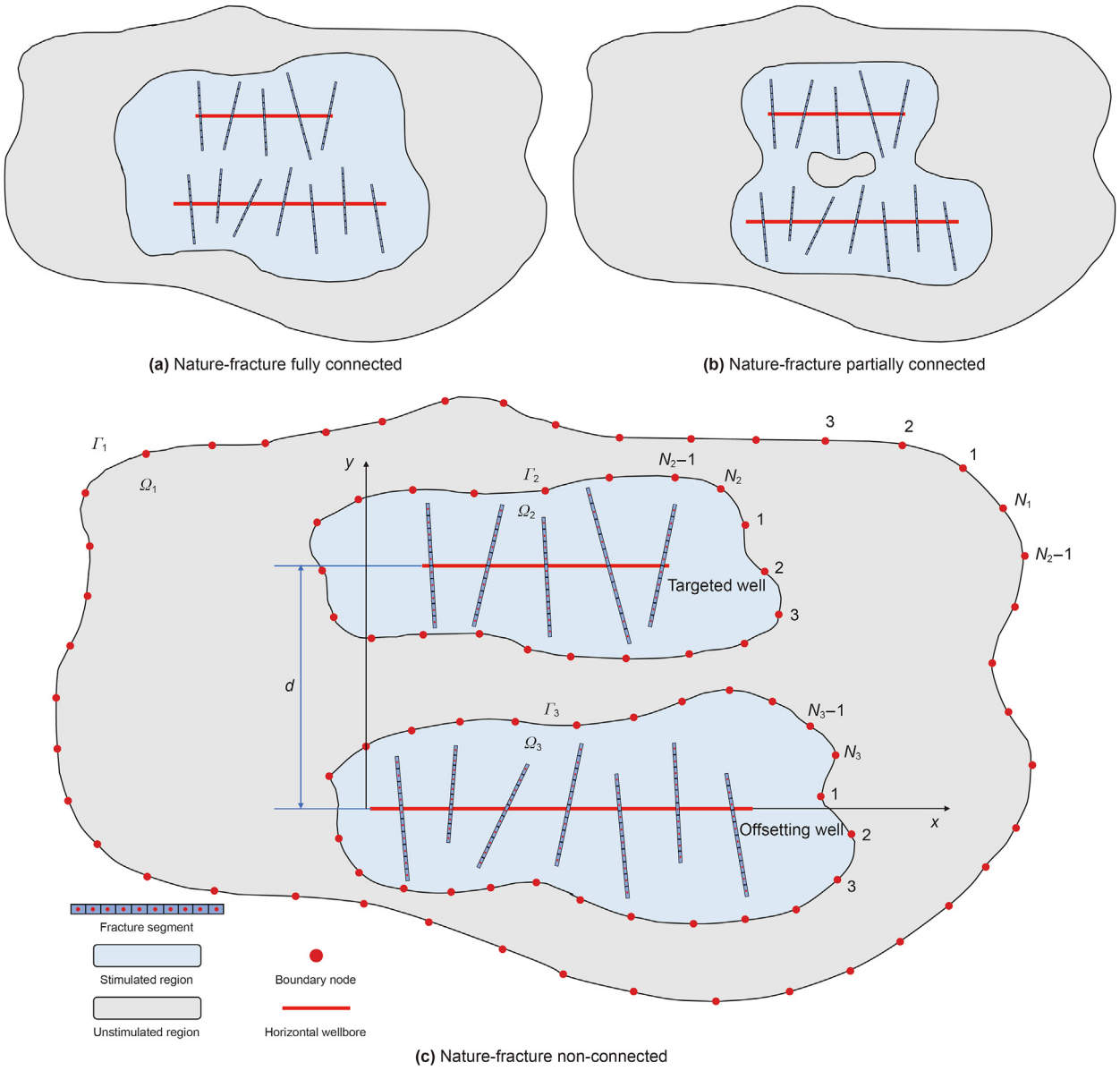

Fig. 2. The schematic diagram of the communication status of nature-fractures in multi-well pads.

$$S_w = 1 - \left(1 - \frac{h_w}{r}\right)^2 \tag{10}$$

where S_w is the water saturation of the matrix.

According to Eqs. (9) and (10), the apparent permeability of the inorganic pores with the impact of the bound water film considered can be obtained

$$k_{\text{app-iom}} = (1 - S_w)k_m \tag{11}$$

where $k_{\text{app-iom}}$ is the apparent permeability of the inorganic pores, m^2.

According to Li et al. (2018), if we consider the non-homogeneous nature of the core, the tendency of bound water to block the pore throat, leading to a substantial reduction in the seepage capacity of the core, is there:

$$k_{\text{app-iom}} = (1 - S_w)^{2\kappa}k_m \tag{12}$$

where κ is the equivalent pore size correction factor, taking into account the effect of water content. The value of κ ranges from 0.5 to 2 and the exact value can be determined according to the digital core and core pore throat structure.

The apparent permeability of the shale matrix considering organic and inorganic pores is

$$k_{\text{app}} = \varphi k_{\text{app-or}} + (1 - \varphi)k_{\text{app-iom}} \tag{13}$$

where φ is the percentage of organic pores; k_{app} is the apparent permeability of the shale matrix, m^2.

3. Model establishment and solution

3.1. Physical model

As shown in Fig. 2(c), the reservoir contains two MFHWs, i.e. the targeted well and the offsetting well, with the SRV regions distributed around each MFHW. Here, Γ represents the boundary of the region, and Ω represents the region. The model is solved using the multi-connected boundary element method. The assumptions for the model are as follows.

(1) The reservoir contains a single-phase gas flow, which satisfies Darcy's law.
(2) Hydraulic fractures are considered finite-conductivity and are influenced by stress-sensitive effects.
(3) The effects of gravity and capillary forces are neglected.
(4) The top and bottom of the reservoir are sealed, and the outer boundary (Γ_1) is closed.
(5) The SRV region is considered a dual medium consisting of matrix porosity and nature-fractures, while the uSRV region is considered a single medium.
(6) Bound water film exists only in inorganic pores.

3.2. Mathematical model

3.2.1. Reservoir flow equations

Dimensionless distances are expressed as follows:

$$x_D = \frac{x}{L}$$

$$y_D = \frac{y}{L}$$

$$r_D = \sqrt{{x_D}^2 + {y_D}^2}$$

$$S_{Di,j} = \frac{S_{i,j}}{L}$$

$$H_{Di,j} = \frac{H_{i,j}}{L}$$

Dimensionless pseudo-pressure is

$$m_D = \frac{\pi k h T_{sc}}{q_{sc} p_{sc} T}(m_i - m)$$

Dimensionless line density flow is

$$q_{Di,j} = \frac{L q_{sci,j}}{q_{sc}}$$

Dimensionless time is

$$t_D = \frac{k}{\mu_{gi}\left(\phi_f c_f + \phi_m c_m\right)L^2} t$$

Dimensionless permeability modulus is

$$\gamma_D = \frac{p_{sc} q_{sc} T}{\pi k h T_{sc}} \gamma$$

Dimensionless fracture conductivity is

$$R_{FD} = \frac{k_F w_F}{kL}$$

Dimensionless wellbore storage coefficient is

$$C_D = \frac{C}{2\pi h\left(\phi_f c_f + \phi_m c_m\right)L^2}$$

Definition of other parameters are

$$c_d = \frac{2Tp_{sc}}{\phi_m \mu_{gi} T_{sc}} \frac{\left(1 - \phi_f - \phi_m\right)G_L m(p_L)}{[m(p_L) + m(p)]^2}$$

$$\omega = \frac{\phi_f c_f}{\phi_f c_f + \phi_m c_m}$$

$$\omega_d = \frac{\phi_m c_d}{\phi_f c_f + \phi_m c_m}$$

$$\sigma = \frac{k_f(\phi_F c_F)}{k_F\left(\phi_f c_f + \phi_m c_m\right)}$$

$$\lambda = \alpha \frac{k_m}{k_f} L^2$$

$$M = \frac{k_m}{k_f}$$

$$\eta = \frac{k_m\left(\phi_f c_f + \phi_m c_m\right)}{k_f(\phi_m c_m)}$$

$$\chi = \frac{k_{app}}{k_m}$$

where L is the reference length, m; $S_{i,\,j}$ is the length of the j-th segment of the i-th fracture in the horizontal well, m; $H_{i,\,j}$ is the distance from the horizontal well to the j-th segment of the i-th fracture, m; p_{sc} is the atmospheric pressure at surface conditions, Pa; q_{sc} is the well production at surface conditions, m^3/s; T_{sc} is the temperature at surface conditions, K; m_i is the initial pseudo-pressure of the reservoir, Pa/s; h is the reservoir thickness, m; m is the pseudo-pressure, Pa/s; $q_{sci,j}$ is the line density of flow rate of the j-th segment of the i-th hydraulic fracture in the horizontal well, m^2/s; μ_{gi} is the initial viscosity of shale gas, Pa·s; ϕ_f is the porosity of the nature fracture; ϕ_m is the porosity of the matrix; ϕ_F is the porosity of the hydraulic fracture; c_f is the compressibility factor of the nature fracture, Pa^{-1}; c_m is the compressibility factor of the matrix, Pa^{-1}; c_F is the compressibility factor of the hydraulic fracture, Pa^{-1}; t is the time, s; γ is the hydraulic fracture permeability modulus, $Pa\cdot s/Pa^2$; k_f is the permeability of nature fracture, m^2; k_F is the permeability of hydraulic fracture, m^2; w_F is the hydraulic fracture width, m; C is the well storage coefficient, m^3·Pa; α is the shape factor, m^{-2}.

According to Langmuir isothermal adsorption equation, the desorption gas q_{des} can be expressed as

$$q_{des} = \rho_g\left(1 - \phi_f - \phi_m\right)G_L \frac{m(p_L)}{(m(p_L) + m(p))^2} \frac{\partial m(p)}{\partial t} \tag{14}$$

Using the point source function method (Gringarten and Ramey, 1973, 1974), while introducing pseudo-pressure, dimensionless

variables, and Laplace transformation, we can obtain the inner and outer zone control equations.

The control equation of the outer zone is as follows:

$$\frac{\partial^2 \overline{m}_{\mathrm{mD}}}{\partial x_{\mathrm{D}}^2}+\frac{\partial^2 \overline{m}_{\mathrm{mD}}}{\partial y_{\mathrm{D}}^2}=s\overline{m}_{\mathrm{mD}} \tag{15}$$

where s is the Laplace variable; $\overline{m}_{\mathrm{mD}}$ is the dimensionless pseudo-pressure of the matrix in the Laplace domain;

Considering the pseudo-steady flow from pores to fractures, the control equation of the SRV region around the MFHWs is as follows:

$$\frac{\partial^2 \overline{m}_{\mathrm{fD}}}{\partial x_{\mathrm{D}}^2}+\frac{\partial^2 \overline{m}_{\mathrm{fD}}}{\partial y_{\mathrm{D}}^2}=\eta\left[s\omega\overline{m}_{\mathrm{fD}}+s(1-\omega+\omega_{\mathrm{d}})\overline{m}_{\mathrm{mD}}\right]-2\pi M\int_{\Omega}\overline{q}_{\mathrm{D}i,j}\delta\left(x-x_{i,j},y-y_{i,j}\right)\mathrm{d}S \tag{16}$$

The crossflow is

$$\chi\lambda\left(\overline{m}_{\mathrm{mD}}-\overline{m}_{\mathrm{fD}}\right)+s\eta(1-\omega+\omega_{\mathrm{d}})\overline{m}_{\mathrm{mD}}=0 \tag{17}$$

$$u=\begin{cases} s & \text{uSRV region} \\ s\eta\left[\omega+\dfrac{\chi\lambda(1-\omega+\omega_{\mathrm{d}})}{\chi\lambda+\eta s(1-\omega+\omega_{\mathrm{d}})}\right] & \text{SRV region}\end{cases} \tag{23}$$

where $\overline{m}_{\mathrm{fD}}$ is the dimensionless pseudo-pressure of the nature fracture in the Laplace domain; $\overline{q}_{\mathrm{D}i,j}$ is the dimensionless flow rate of the j-th segment of the i-th hydraulic fracture in the horizontal well in the Laplace domain; $(x_{i,j}, y_{i,j})$ is the discrete segment coordinates of the hydraulic fracture; $\delta()$ is the Dirac function; n is the normal vector of the boundary; $K_0()$ is the zeroth-order Bessel function.

The outer boundary Γ_1 of the reservoir can be discretized into N_1 linear segments, while the inner boundaries Γ_2 and Γ_3 can be discretized into N_2 and N_3 linear segments, respectively. For the outer zone, the numbering and integration order of the boundary discretization are as shown in Fig. 3(a), while for the inner zone, the numbering and integration order is as shown in Fig. 3(b).

Based on the boundary element method, the boundary integral equation for an arbitrary point k in Laplace space in the outer zone is

$$\theta\overline{m}_{\mathrm{mD}}(Q_{\mathrm{k}},s)=\frac{1}{2\pi}\sum_{n=1}^{N_1+N_2+N_3}\frac{l_n}{2}\int_{-1}^{1}\left[E(P',Q_{\mathrm{k}},u)\left(\frac{1-\xi}{2}\frac{\partial\overline{m}_{\mathrm{mD},n}}{\partial n}+\frac{1+\xi}{2}\frac{\partial\overline{m}_{\mathrm{mD},n+1}}{\partial n}\right)-\left(\frac{1-\xi}{2}\overline{m}_{\mathrm{mD},n}+\frac{1+\xi}{2}\overline{m}_{\mathrm{mD},n+1}\right)\frac{\partial E(P',Q_{\mathrm{k}},u)}{\partial n}\right]\mathrm{d}\xi \tag{24}$$

The initial conditions are

$$\overline{m}_{\mathrm{mD}}|_{t_{\mathrm{D}}=0}=\overline{m}_{\mathrm{fD}}\Big|_{t_{\mathrm{D}}=0}=0 \tag{18}$$

The boundary conditions at the outer boundary are

$$\frac{\partial\overline{m}_{\mathrm{mD}}}{\partial n}=0 \tag{19}$$

The conditions at the interface between the inner and outer zones are

$$\frac{\partial\overline{m}_{\mathrm{mD}}}{\partial n}=-\frac{1}{M}\frac{\partial\overline{m}_{\mathrm{fD}}}{\partial n}\quad(x_{\mathrm{D}},y_{\mathrm{D}})\in\Gamma_2,\Gamma_3 \tag{20}$$

$$\overline{m}_{\mathrm{mD}}=\overline{m}_{\mathrm{fD}}\quad(x_{\mathrm{D}},y_{\mathrm{D}})\in\Gamma_2,\Gamma_3 \tag{21}$$

The fundamental solution in Laplace space using the boundary element method is

$$E(P,Q,u)=K_0\left(r_{\mathrm{D}}(P,Q)\sqrt{u}\ \right) \tag{22}$$

where P and Q represent arbitrary points inside or on the boundary of the domain.

The boundary integral equation in the SRV region is

$$\theta\overline{m}_{\mathrm{fD}}(Q_{\mathrm{k}},s)=\frac{1}{2\pi}\sum_{n=1}^{N_2,N_3}\frac{l_n}{2}\int_{-1}^{1}\left[E(P',Q_{\mathrm{k}},u)\left(\frac{1-\xi}{2}\frac{\partial\overline{m}_{\mathrm{fD},n}}{\partial n}+\frac{1+\xi}{2}\frac{\partial\overline{m}_{\mathrm{fD},n+1}}{\partial n}\right)-\left(\frac{1-\xi}{2}\overline{m}_{\mathrm{fD},n}+\frac{1+\xi}{2}\overline{m}_{\mathrm{fD},n+1}\right)\frac{\partial E(P',Q_{\mathrm{k}},u)}{\partial n}\right]\mathrm{d}\xi+\sum_{i=1}^{FN}\times\sum_{j=1}^{W}\int_{S_{\mathrm{D}i,j}}\overline{q}_{\mathrm{D}i,j}E(P',Q_k,u)\mathrm{d}S \tag{25}$$

where Q_{k} is the point inside or on the boundary; P' is the point on the boundary; l_{n} is the dimensionless length of the n-th segmented boundary section; FN is the total number of fractures in the SRV region; W is the number of discretized segments for each fracture; and θ is a constant related to the geometry at point Q_{k}.

$$\theta=\begin{cases}1/2 & \text{for points on smooth parts of boundary}\\ \beta/2\pi & \text{for points on non-smooth parts of boundary}\\ 1 & \text{for points in internal domain}\end{cases} \tag{26}$$

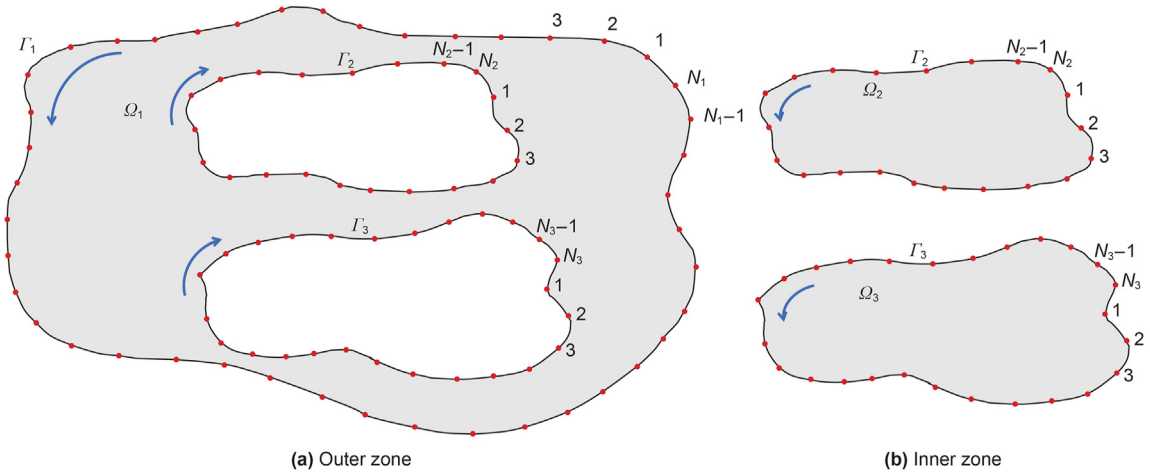

Fig. 3. The schematic diagram of numbering and integration order of boundary.

where β represents the angle of the boundary point Q_k.

Similarly, the boundary integral equation for the center point of discretized fracture segments in the inner zone is

$$\overline{m}_{\mathrm{FD}i,j}=\frac{1}{2\pi}\sum_{n=1}^{N_2,N_3}\frac{l_n}{2}\int_{-1}^{1}\left[E(P',Q_{\mathrm{F}},u)\left(\frac{1-\xi}{2}\frac{\partial\overline{m}_{\mathrm{fD},n}}{\partial n}+\frac{1+\xi}{2}\frac{\partial\overline{m}_{\mathrm{fD},n+1}}{\partial n}\right)-\left(\frac{1-\xi}{2}\overline{m}_{\mathrm{fD},n}+\frac{1+\xi}{2}\overline{m}_{\mathrm{fD},n+1}\right)\frac{\partial E(P',Q_{\mathrm{F}},u)}{\partial n}\right]\mathrm{d}\xi+\sum_{i=1}^{FN}\times\sum_{j=1}^{W}\int_{S_{\mathrm{D}i,j}}\overline{q}_{\mathrm{D}i,j}E(P',Q_{\mathrm{F}},u)\mathrm{d}S \tag{27}$$

where $\overline{m}_{\mathrm{FD}i,j}$ represents the dimensionless pseudo-pressure at the midpoint of the j-th discretized segment of the i-th hydraulic fracture; Q_{F} represents the midpoint of discretized segments of hydraulic fractures in the inner zone.

3.2.2. Fracture flow equations

Considering the stress sensitivity of hydraulic fractures, the fracture control equation is obtained using an exponential form of permeability variation:

$$\frac{\partial}{\partial x_{\mathrm{D}}}\left(\mathrm{e}^{-\gamma_{\mathrm{D}}(m_{\mathrm{FDi}}-m_{\mathrm{FD}})}\frac{\partial m_{\mathrm{FD}}}{\partial x_{\mathrm{D}}}\right)+\frac{\partial}{\partial y_{\mathrm{D}}}\left(\mathrm{e}^{-\gamma_{\mathrm{D}}(m_{\mathrm{FDi}}-m_{\mathrm{FD}})}\frac{\partial m_{\mathrm{FD}}}{\partial y_{\mathrm{D}}}\right)=\sigma\frac{\partial m_{\mathrm{FD}}}{\partial t_{\mathrm{D}}} \tag{28}$$

where γ_{D} is the dimensionless permeability modulus of hydraulic fracture.

By using the Pedrosa variable substitution and perturbation transformation, combined with Eq. (28), we obtain

$$\nabla^2\psi_{\mathrm{FD}}=\sigma\frac{\partial\psi_{\mathrm{FD}}}{\partial t_{\mathrm{D}}} \tag{29}$$

where Ψ_{FD} satisfies the following equation:

$$m_{\mathrm{FD}}=-\frac{1}{\gamma_{\mathrm{D}}}\ln(1-\gamma_{\mathrm{D}}\psi_{\mathrm{FD}}) \tag{30}$$

In Laplace space, discretization of the fracture model yields

$$\overline{\psi}_{\mathrm{wD}}-\overline{\psi}_{\mathrm{FD}i,j}=\frac{2\pi}{R_{\mathrm{FD}}}\left\{H_{\mathrm{D}i,j}\sum_{n=1}^{j}\overline{q}_{\mathrm{D}i,n}S_{\mathrm{D}i,n}-\left[\sum_{n=1}^{j-1}\overline{q}_{\mathrm{D}i,n}(j-n)S_{\mathrm{D}i,n}{}^2+\overline{q}_{\mathrm{D}i,j}\frac{S_{\mathrm{D}i,j}{}^2}{8}\right]\right\} \tag{31}$$

3.3. Model solution

For this model, the unknowns include the pseudo-pressure at boundary points and internal points, the flow rate on fracture

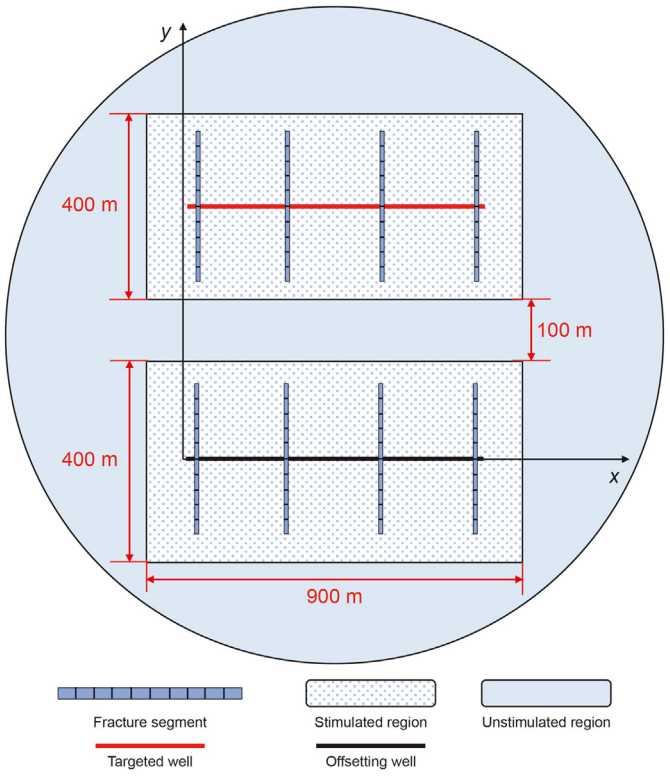

Fig. 4. The schematic diagram of the simplified model.

Table 1
Parameter values of the simplified model.

Group	Item	Value	Unit
Basic parameters	Initial reservoir pressure	35	MPa
	Reservoir thickness	35	m
	Rock compressibility	4.35×10^{-4}	MPa^{-1}
	Langmuir isothermal adsorption pressure	4	MPa
	Langmuir isothermal adsorption volume	10	m^3/m^3
SRV region	Matrix permeability	0.05	mD
	Porosity of the macro pore system	0.1	–
	The length of the targeted well's SRV x_e	900	m
	The width of the targeted well's SRV y_e	400	m
	The length of the offsetting well's SRV x_m	900	m
	The length of the offsetting well's SRV y_m	400	m
uSRV region	Matrix permeability	0.02	mD
	Porosity of the macro pore system	0.08	–
	Unstimulated region radius	4000	m
Hydraulic fracture	Fracture conductivity	200	mD·m
	Fracture half length	80	m
	Fracture dip angle	90	°
Well	Well number	2	–
	Well length	750	m
	Well radius	0.1	m
	Well spacing	500	m
	Skin factor	0	–
	Wellbore storage coefficient	0	m^3/MPa
	Targeted well production rate	1	m^3/d
	Offsetting well production rate	1	m^3/d
Fluid	Viscosity	0.25	mPa·s
	Compressibility	0.018	MPa^{-1}

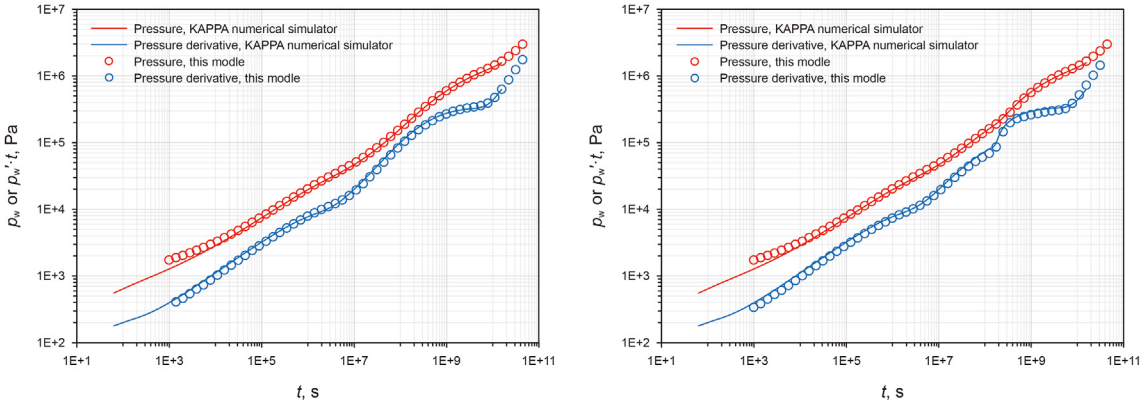

(a) Two wells producing simultaneously

(b) Offsetting well producing five years later

Fig. 5. Comparing results between the numerical model and our model.

segments, the pseudo-pressure on fracture segments, and the pseudo-pressure at the bottom of the horizontal well. The pseudo-pressure coefficients at boundary points and internal points can be obtained from Eqs. (24) and (25). The pseudo-pressure coefficients on fracture segments can be obtained from Eq. (27), and the relationship between the flow rate and the pseudo-pressure is represented by the discretized formula of the fracture model Eq. (31).

In addition, the constant production condition for the targeted well is expressed as

$$\sum_{i=1}^{FN}\sum_{j=1}^{W} S_{\mathrm{D}i,j}\bar{q}_{\mathrm{D}i,j} = \frac{1}{s} \tag{32}$$

The constant production condition for the offsetting well is expressed as

$$\sum_{i=1}^{FN}\sum_{j=1}^{W} S_{\mathrm{D}i,j}\bar{q}_{\mathrm{D}i,j} = \frac{q_{\mathrm{offsetting}}}{q_{\mathrm{targeted}}}\frac{1}{s} \tag{33}$$

By combining Eqs. (24), (25), (27), and (31)–(33), we can obtain the coefficient matrix. Solving it yields the bottom-hole pressure ($\bar{\psi}_{\mathrm{wD}}$) of the targeted well:

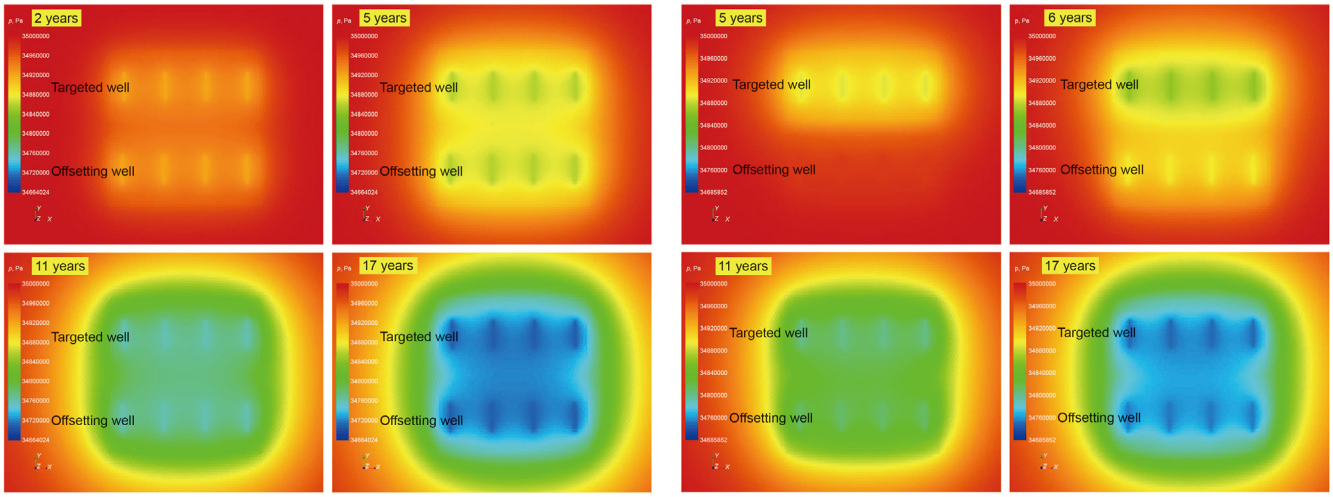

Fig. 6. Pressure profile of the multi-well horizontal pad.

Table 2
Parameter values of the model.

Group	Item	Value	Unit
Basic parameters	Initial reservoir pressure	35	MPa
	Reservoir thickness	35	m
	Rock compressibility	4.35×10^{-4}	MPa^{-1}
	Langmuir isothermal adsorption pressure	4	MPa
	Langmuir isothermal adsorption volume	10	m^3/m^3
SRV region	Matrix permeability	0.001	mD
	Nature-fracture permeability	0.1	mD
	Porosity of the macro pore system	0.1	–
	Porosity of the fracture system	0.03	–
	The length of the targeted well's SRV x_e	900	m
	The width of the targeted well's SRV y_e	400	m
	The length of the offsetting well's SRV x_m	900	m
	The length of the offsetting well's SRV y_m	400	m
	Constrained water saturation	10	%
	Geometry factor	1×10^{-5}	m^{-2}
uSRV region	Matrix permeability	0.001	mD
	Porosity of the macro pore system	0.1	–
	Unstimulated region radius	4000	m
Hydraulic fracture	Fracture conductivity	200	mD·m
	Fracture half length	80	m
	Fracture dip angle	90	°
Well	Well number	2	–
	Well length	750	m
	Well radius	0.1	m
	Well spacing	500	m
	Skin factor	0.0001	–
	Wellbore storage coefficient	1	m^3/MPa
	Targeted well production rate	1	m^3/d
	Offsetting well production rate	1	m^3/d
Fluid	Viscosity	0.25	mPa·s
	Compressibility	0.018	MPa^{-1}

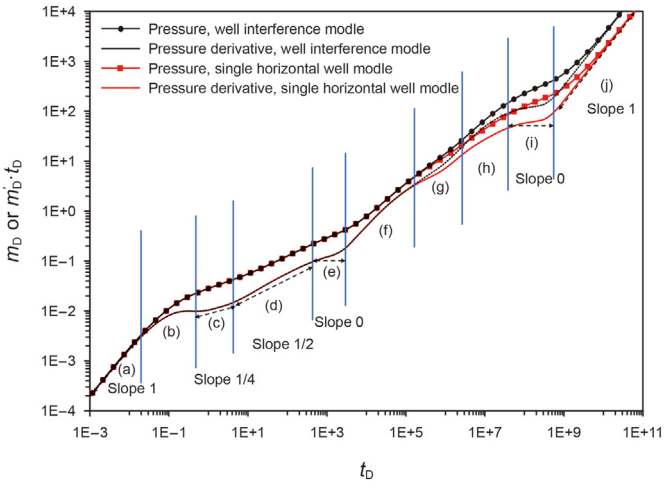

Fig. 7. Integrated flow regimes of the multi-well horizontal pad without nature-fracture communication.

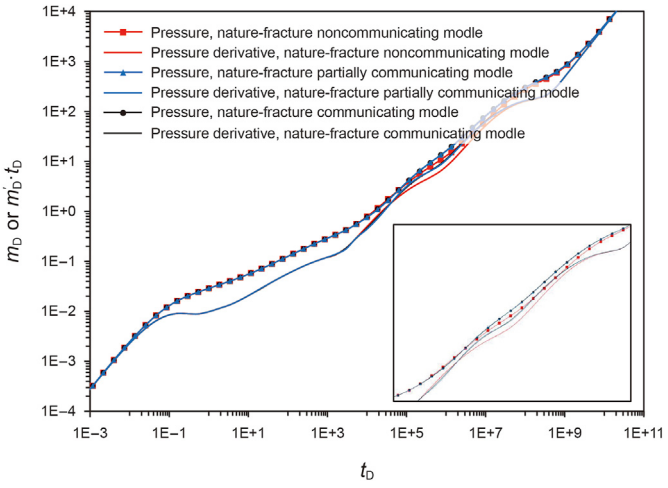

Fig. 10. Effect of SRV region communication status on the type curve of the targeted well in the multi-well horizontal pad ($q_{targeted}$: $q_{offsetting}$ = 1:2).

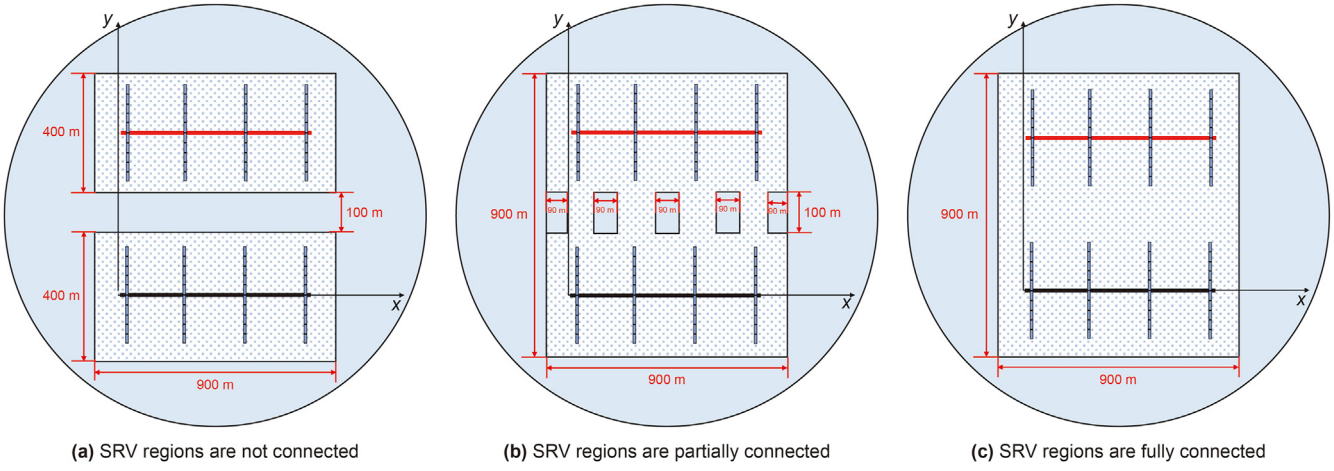

Fig. 8. The schematic diagram of three different models.

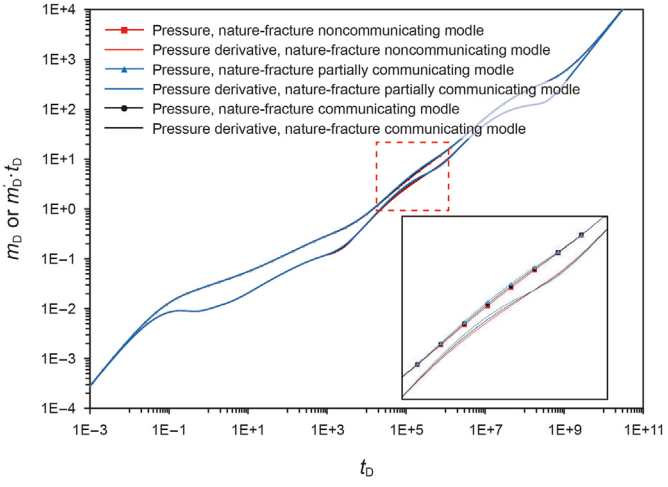

Fig. 9. Effect of SRV region communication status on the type curve of the targeted well in the multi-well horizontal pad ($q_{targeted}$: $q_{offsetting}$ = 1:1).

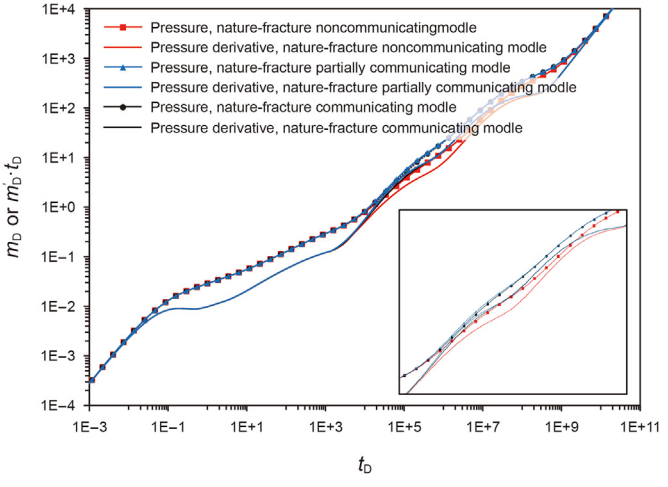

Fig. 11. Effect of SRV region communication status on the type curve of the targeted well in the multi-well horizontal pad ($q_{targeted}$: $q_{offsetting}$ = 2:1).

$$\begin{bmatrix} A_{1,N_{total}\times N_{total}} & 0 & B_{1,N_{total}\times F_{total}} & 0 \\ 0 & A_{2,F_{total}\times F_{total}} & B_{2,F_{total}\times F_{total}} & 0 \\ 0 & D_{F_{total}\times F_{total}} & E_{F_{total}\times F_{total}} & I_{F_{total}\times 2} \\ 0 & 0 & i_{2\times F_{total}} & 0 \end{bmatrix} \times \begin{bmatrix} \overline{m}_{BD,N_{total}\times 1} \\ \overline{m}_{FD,F_{total}\times 1} \\ \overline{q}_{FD,F_{total}\times 1} \\ \overline{m}_{wD,2\times 1} \end{bmatrix} = \begin{bmatrix} 0_{(N_{total}+2F_{total})\times 1} \\ \frac{1}{s} \\ \frac{q_{offsetting}}{q_{targeted}}\frac{1}{s} \end{bmatrix} \tag{34}$$

where A is the solution of the seepage control equations for the inner and outer zones; B is the solution of the line source equations of discrete fracture; D and E are the solutions of the seepage control equations for the hydraulic fracture; I is the unit matrix; i is a matrix with element 1.

Taking into account wellbore storage effects and skin effects, we obtain

$$\overline{\psi}^{*}_{wD} = \frac{s\overline{\psi}_{wD} + S_k}{s + C_D s^2 (s\overline{\psi}_{wD} + S_k)} \tag{35}$$

Finally, using the Stehfest numerical inversion algorithm, we obtain the pseudo-pressure in real space. Then, using Eq. (30), we calculate the pseudo-pressure at the bottom of the well considering the stress sensitivity of the hydraulic fractures.

If it is necessary to set the production time for the horizontal well, the pressure superposition principle can be employed to

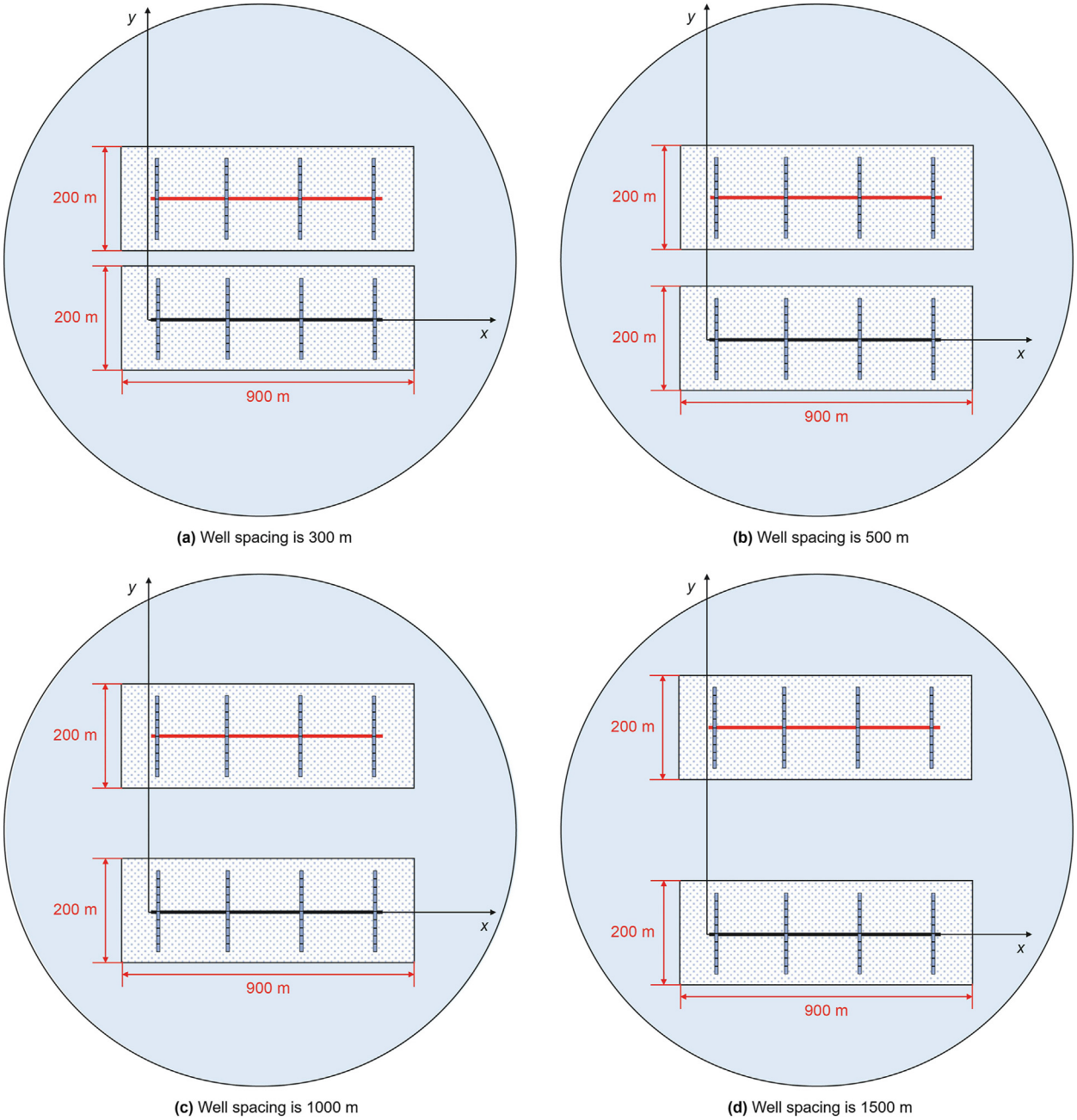

Fig. 12. The schematic diagram of the multi-well horizontal pad with various well spacing.

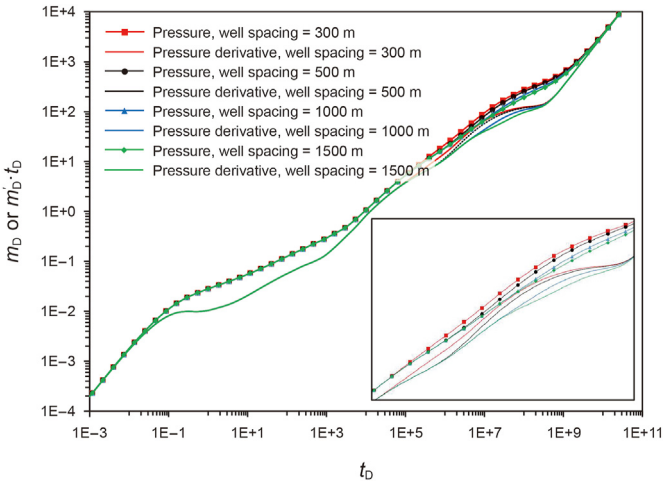

Fig. 13. Effect of various well spacings on the type curve of the targeted well in the multi-well horizontal pad.

address the impact of different production times of the offsetting well on the targeted well. This method allows for setting different initial production times for different wells in the model. The targeted well and the offsetting well can have different production capacities at different time intervals. When the production capacity is set as 0, it indicates that the well does not produce during that time interval.

4. Model validation

The model was validated using a simplified model (Fig. 4) and with the assistance of Saphir well-testing software. In the simplified model, the outer boundary is circular and closed, each hydraulic fractured horizontal well has an independent SRV region, and the reservoir is considered as a single medium. Other parameters are as shown in Table 1.

The model is divided into two cases for validation: simultaneous production from two hydraulic fractured horizontal wells and production from two hydraulic fractured horizontal wells with staggered production schedules. The validation results are shown in Fig. 5, which indicate that the results from our model are consistent with those from numerical simulations, validating the reliability of our model calculations. As shown in the pressure profile generated by Saphir (Fig. 6), when the offsetting well begins production five years later, the interwell interference on the targeted well during the early and mid-production stages is less than in the case where both wells produce simultaneously. However, in the late production stage, the interwell interference on the targeted well becomes similar in both scenarios. It can also be observed that even if the SRV regions generated by the two fractured horizontal wells are not connected, the interference between the two wells is significant and increases over time.

5. Results and discussion

We established different models to perform flow stage division and sensitivity analysis, with the SRV region set as a dual-porosity medium and the uSRV region set as a single-porosity medium. Other parameters are shown in Table 2.

5.1. Flow regimes

As shown in Fig. 7, the transient behavior of the multi-well horizontal pad with individual SRVs can be divided into ten flow regimes.

(a) Wellbore storage stage

In the log-log plot, the bottom-hole pressure and pressure derivative during the wellbore storage stage are displayed as straight lines with unit slope.

(b) Transition stage from wellbore storage to bilinear flow

In this stage, the pressure derivative curve exhibits a “convex” shape, and the degree of convexity in this region depends on the skin value.

(c) Bilinear flow stage

The pressure and pressure derivative curves are displayed as straight lines with a slope of 1/4 in the log-log plot.

(d) Linear flow stage

The pressure and pressure derivative curves are displayed as straight lines with a slope of 1/2 in the log-log plot.

(e) Pseudo-radial flow stage

The horizontal well forms a radial flow within the SRV region, and this stage changes with the size of the SRV region. The pressure and pressure derivative curves are displayed as straight lines with a slope of 1/2 in the log-log plot.

(f) Stage of transitional flow between the SRV region and the uSRV region

In this stage, there is a noticeable increase in pressure and pressure derivative, and the magnitude of this increase is influenced by the flow rate ratio between the SRV region and the uSRV region.

(g) Stage of SRV region matrix pore fluid flowing into nature-fractures

The concave trend formed by the matrix pore fluid flowing into the nature-fractures, the degree of concavity depends on the ratio of matrix pore volume to nature-fracture pore volume in the SRV region.

(h) Well interference flow stage

During this stage, interference from the offsetting well affects the production of the targeted well, increasing both pressure and pressure derivative curves. Since the timing of interwell interference is related to well spacing, reservoir properties, and the connectivity of the SRV region, the interwell interference stage may occur earlier or later under different conditions, causing this stage to overlap with other flow stages.

(i) Radial flow stage

In this stage, the pressure derivative curve is displayed as a horizontal line in the log-log plot, and its value is influenced by the transmissibility ratio between the SRV region and the uSRV region, as well as the production from the offsetting well.

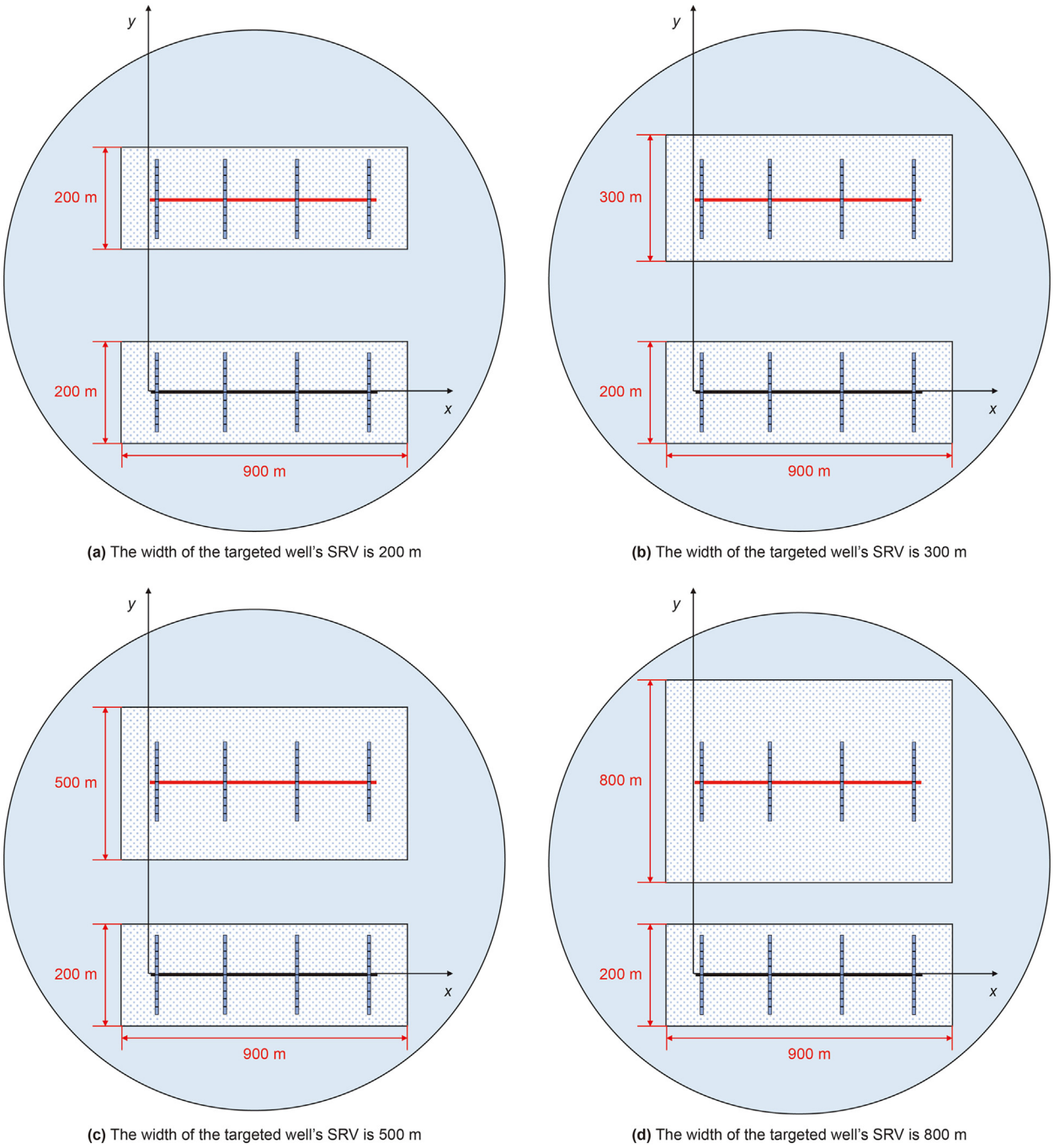

(a) The width of the targeted well's SRV is 200 m

(b) The width of the targeted well's SRV is 300 m

(c) The width of the targeted well's SRV is 500 m

(d) The width of the targeted well's SRV is 800 m

Fig. 14. The schematic diagram of the multi-well horizontal pad with different sizes of the targeted well's SRV region (the well spacing is 600 m).

(j) Boundary-dominated flow stage

In this stage, the pressure and pressure derivative curves appear as straight lines with a slope of 1 in the log-log plot.

5.2. Comparison and sensitivity analysis

5.2.1. Effect of SRV region connectivity

To investigate the impact of SRV area connectivity on the production of the targeted well in a multi-well horizontal pad, we established three models with different degrees of SRV connectivity (Fig. 8), and sensitivity was analyzed with varied production capacities of the offsetting well. As shown in Fig. 9, when the production capacities of the targeted well and the offsetting well are equal, the connectivity degree of their SRV regions has minimal impact on the pressure and pressure derivative curves of the targeted well. The reason is that the targeted well and the offsetting well have the same speed and magnitude of pressure wave propagation. Therefore, regardless of the connectivity of the SRV regions, both wells can evenly access the reservoir resources.

When the production capacity of the offsetting well differs from that of the targeted well, the situation changes significantly. When the production capacity of the offsetting well is twice that of the targeted well, the influence of whether the SRV regions are

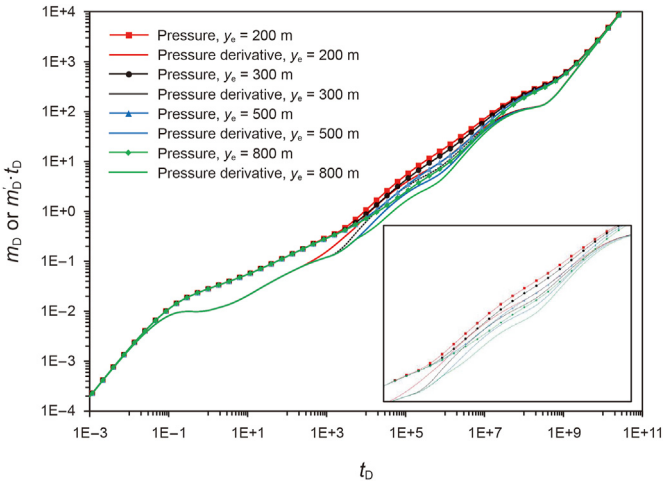

Fig. 15. Effect of different sizes of the targeted well's SRV region on the type curve of the targeted well in the multi-well horizontal pad.

connected to the pressure and pressure derivative curves of the targeted well is illustrated in Fig. 10. Compared to the scenario where the SRV regions are not connected, in the case where the SRV regions are connected, the pressure curve of the targeted well exhibits a significant increase during the transition flow stage and in subsequent stages. The connectivity degree of the SRV regions affects the magnitude of the pressure curve increase during the transition flow stage for the targeted well but does not affect subsequent stages. When the production capacity of the offsetting well is half of that of the targeted well, the impact of whether the SRV regions are connected on the pressure and pressure derivative curves of the targeted well is illustrated in Fig. 11. In comparison to the scenario where the SRV regions are not connected, the connected SRV regions result in a decrease in the pressure curve of the targeted well. The reason for this occurrence lies in the imbalance of production capacities between the two wells, resulting in different speeds and magnitudes of pressure wave propagation between them. Therefore, the SRV region around the well with higher production capacity at the same time forms a larger pressure drop. The connectivity of the SRV regions allows some natural gas from the SRV region around the well with lower production capacity to flow towards the well with higher production capacity to balance the pressure difference. This phenomenon is less pronounced when the SRV regions are not connected.

5.2.2. Effect of well spacing

The spacing of the multi-well horizontal pad directly affects the well interference stage. As the distance between the targeted well and the offsetting well increases (Fig. 12), the occurrence of interference from the offsetting well on the targeted well is delayed, and the pressure derivative curve shifts downward during the interference stage (Fig. 13). Additionally, as the well spacing increases, the targeted well gets closer to the outer boundary, resulting in the radial flow stage becoming less pronounced in the typical pressure curve.

5.2.3. Effect of the size of targeted well's SRV region

The size of the SRV region of the targeted well directly affects the transient behavior of the targeted well during steady-state production. The pressure behavior using different sizes of rectangular boundaries for the targeted well's SRV region was compared (Fig. 14). As shown in Fig. 15, with the expansion of the targeted well's SRV region, the pressure and pressure derivative curves of the targeted well exhibit a trend of dropping during the mid-term production. Additionally, the pseudo-radial flow stage becomes more pronounced. This occurs because the expansion of the SRV region causes a delay in the propagation of pressure waves from the targeted well to the boundary of the SRV region. As a result, the duration of pseudo-radial flow is extended.

5.2.4. Effect of the size of offsetting well's SRV region

To quantify the impact of the offsetting well's SRV region size on the transient behavior of the targeted well, pressure behavior using different sizes of rectangular boundaries for the offsetting well's SRV region was compared (Fig. 16). As shown in Fig. 17, the size of the offsetting well's SRV region mainly affects the production of the targeted well during the interwell interference stage. As the offsetting well's SRV region size increases, the pressure and pressure derivative curves of the targeted well during the interwell interference stage exhibit a trend of initially rising and then dropping. The initial rise is due to the increased interference from the offsetting well's SRV region. However, the subsequent decrease in the pressure curve is attributed to the enlargement of the offsetting well's SRV region, which reduces the pressure consumption caused by steady-state production.

5.2.5. Effect of offsetting well's production capacity

The production rate of the offsetting well directly influences the pressure depletion. Consequently, it has a more significant impact on the transient behavior of the targeted well. As shown in Fig. 18, the dimensionless production rate of the offsetting well ranges from 1 to 4, illustrating the effect of the offsetting well's production rate on the behavior of the targeted well. Different production rates of the offsetting well directly affect the interwell interference stage in the typical pressure curve. As the production rate of the offsetting well increases, the resulting pressure depletion becomes larger, leading to stronger interference with the targeted well. Consequently, the pressure drop required for the targeted well's production during the interwell interference stage increases manifested as a larger amplitude of the pressure and pressure derivative curves in the typical pressure curve of the targeted well.

5.2.6. Effect of the number of hydraulic fractures

As shown in Fig. 19, by maintaining 12 hydraulic fractures in the targeted well and varying the number of hydraulic fractures in the offsetting well, we observe the impact of the number of hydraulic fractures in the offset well on the transient pressure behavior of both the targeted and offsetting wells. In Fig. 20, changes in the number of hydraulic fractures in the offsetting well mainly affect the targeted well during the mid to late production stages. As the number of hydraulic fractures in the offsetting well increases, the interwell interference experienced by the targeted well during these stages becomes more pronounced, leading to a more noticeable upward trend in the pressure and pressure derivative curves. Conversely, as shown in Fig. 21, the impact of changes in the number of hydraulic fractures in the offsetting well on its transient pressure behavior begins in the early stages. As the number of hydraulic fractures in the offsetting well increases, the early-stage pressure and pressure derivative curves of the offsetting well significantly decrease. Additionally, the expanded control area of the offsetting well reduces the interference from the targeted well.

5.2.7. Effect of hydraulic fracture stress sensitivity

Considering the dimensionless permeability modulus of hydraulic fractures to be 0, 0.0005, 0.001, and 0.002, respectively,

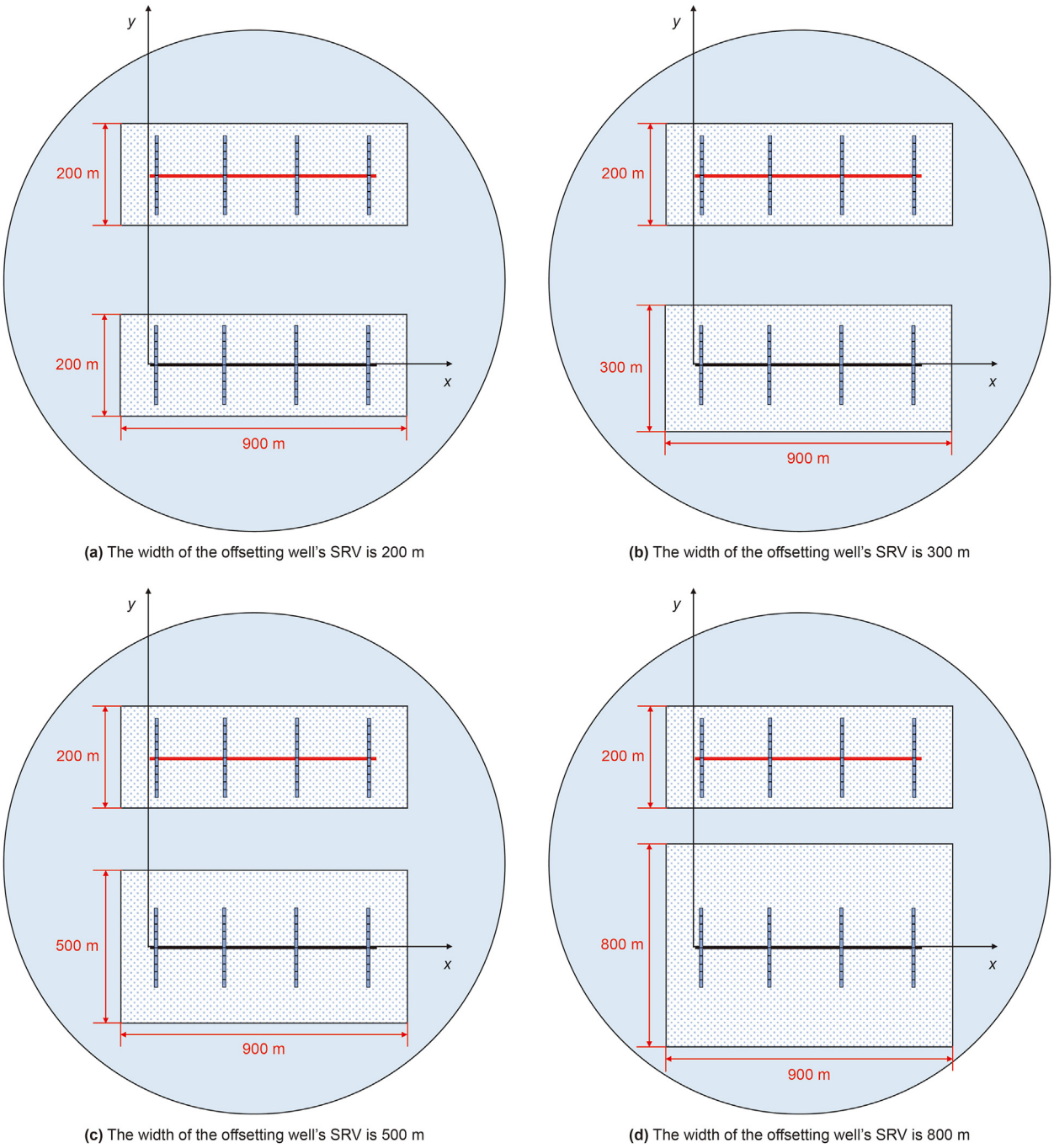

(a) The width of the offsetting well's SRV is 200 m

(b) The width of the offsetting well's SRV is 300 m

(c) The width of the offsetting well's SRV is 500 m

(d) The width of the offsetting well's SRV is 800 m

Fig. 16. The schematic diagram of the multi-well horizontal pad with different sizes of the offsetting well's SRV region (the well spacing is 600 m).

their influence is shown in Fig. 22. Under constant production conditions, the influence of stress sensitivity effect of hydraulic fractures increases as the pressure of hydraulic fractures gradually decreases in the later stages of production. The stronger the stress sensitivity effect (the larger the dimensionless permeability modulus), the greater the upward amplitude of the well test curve in the later stages. Compared to the influence of the offsetting well's production capacity on the targeted well, during the boundary-dominated flow regime, the slope of pressure and pressure derivative curves will be greater than 1 due to the stress sensitivity effect of the hydraulic fracture, whereas under the influence of the offsetting well's production capacity, the slope of the pressure and pressure derivative curves equals 1.

5.2.8. Effect of different production times for the offsetting well

In the production of multi-well horizontal pads, each well often has different production start times. Therefore, it is essential to study the interference between wells under different production schedules. By shifting the production start time of the offsetting well from simultaneous production with the targeted well to 20 years later, the impact on the targeted well's transient behavior is shown in Fig. 23. As the production start time of the offsetting well is delayed, the interference on the targeted well is delayed accordingly, that is manifested by the interference stage of the

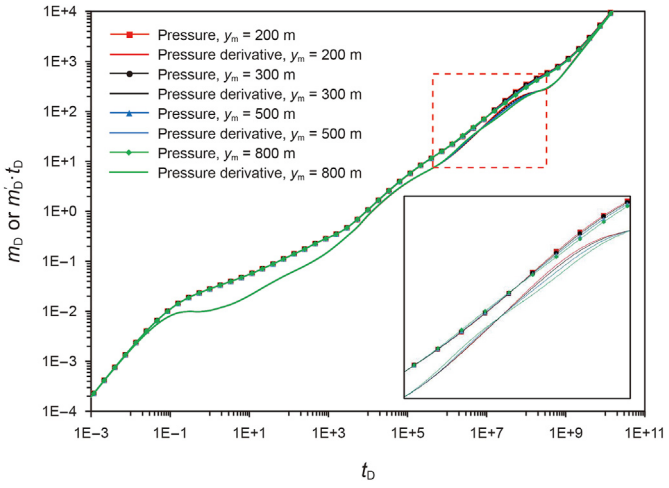

Fig. 17. Effect of different sizes of the offsetting well's SRV region on the type curve of the targeted well in the multi-well horizontal pad.

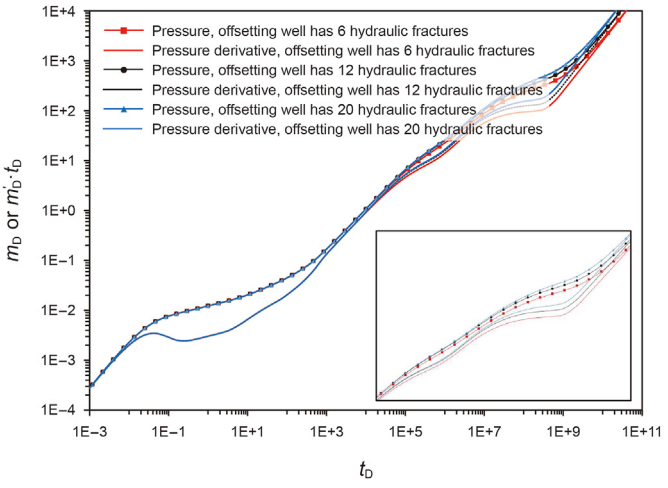

Fig. 20. Effect of different numbers of hydraulic fractures of offsetting well on the type curve of the targeted well in the multi-well horizontal pad.

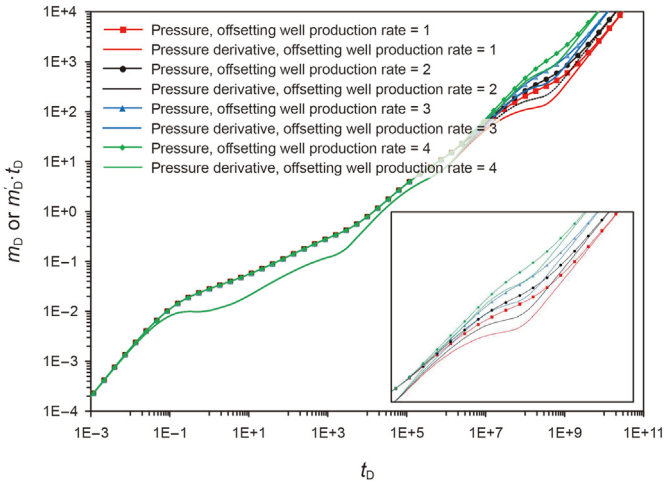

Fig. 18. Effect of different production capacities of the offsetting well on the type curve of the targeted well in the multi-well horizontal pad.

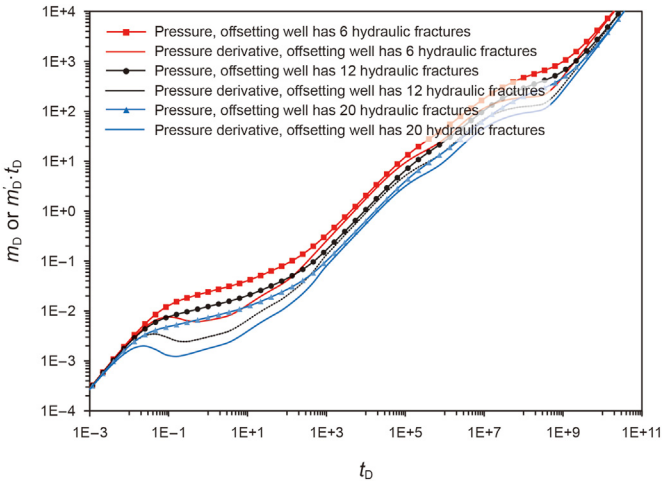

Fig. 21. Effect of different numbers of hydraulic fractures of offsetting well on the type curve of the offsetting well in the multi-well horizontal pad.

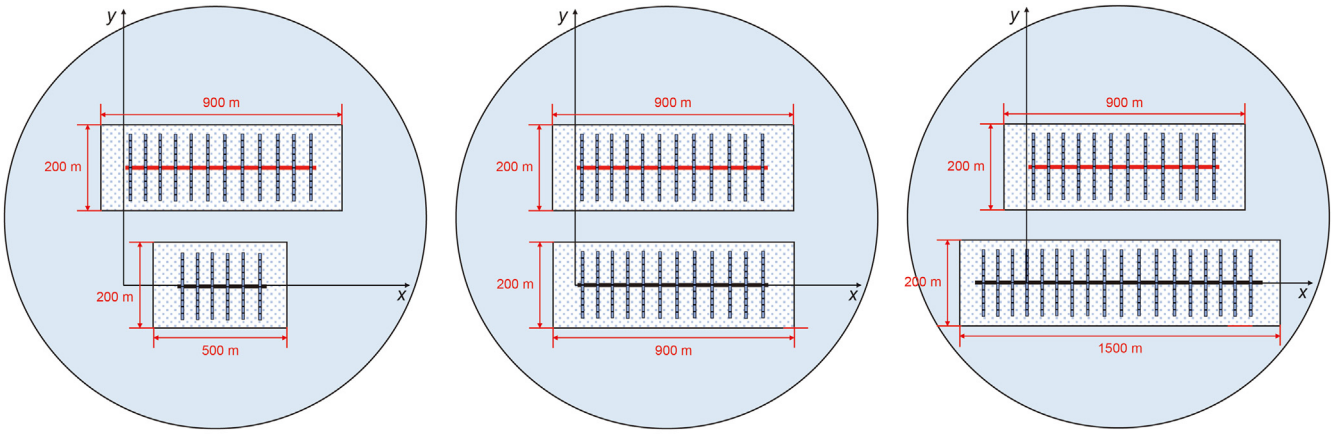

(a) 6 hydraulic fractures in the offsetting well **(b)** 12 hydraulic fractures in the offsetting well **(c)** 20 hydraulic fractures in the offsetting well

Fig. 19. The schematic diagram of the multi-well horizontal pad with different numbers of offsetting well's hydraulic fractures (the well spacing is 220 m).

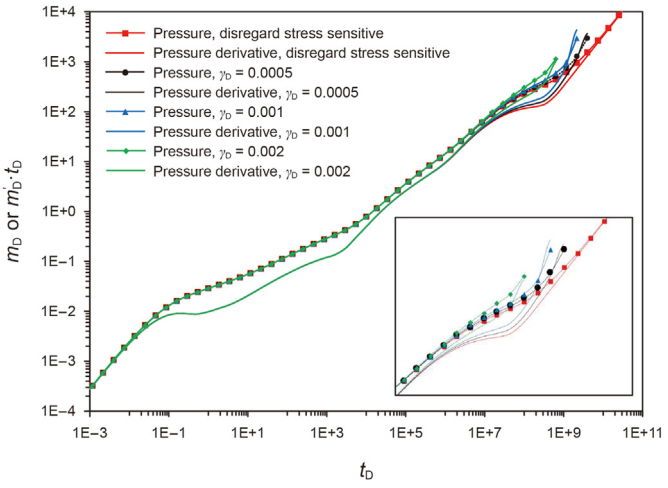

Fig. 22. Effect of hydraulic fracture stress sensitivity on the type curve of the targeted well in the multi-well horizontal pad.

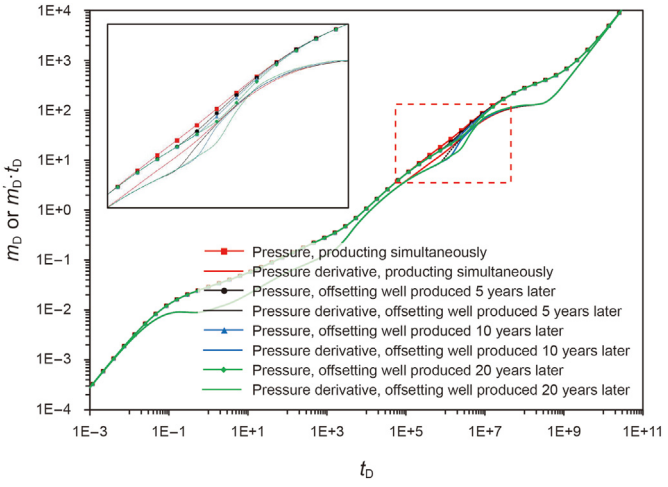

Fig. 23. Effect of different production times for the offsetting well on the type curve of the targeted well in the multi-well horizontal pad.

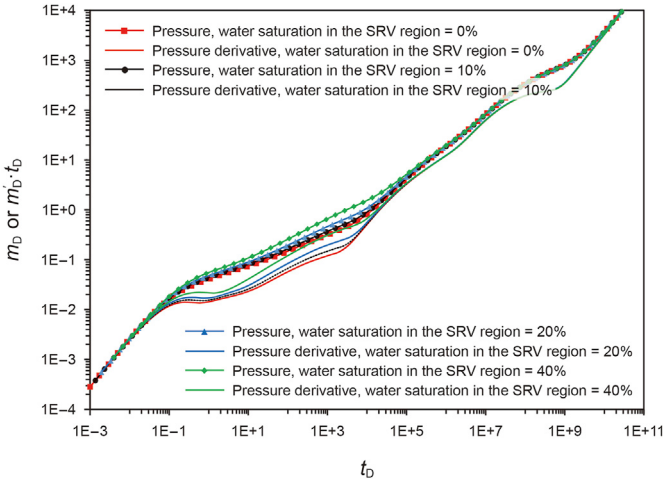

Fig. 24. Effect of different water saturation levels in the SRV region on the type curve of the targeted well in the multi-well horizontal pad.

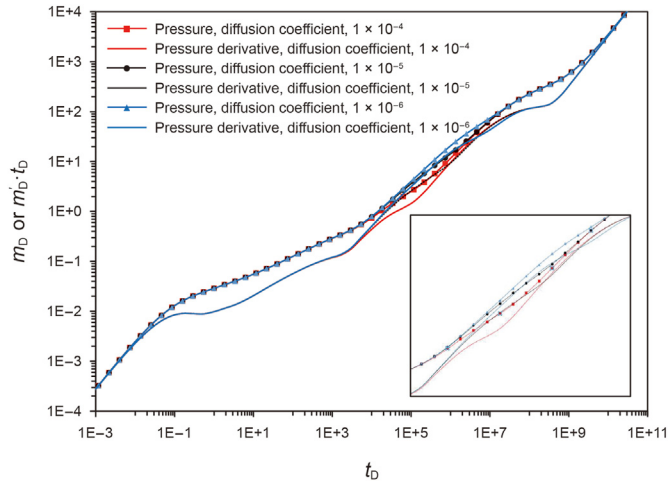

Fig. 25. Effect of different Knudsen diffusion coefficients on the type curve of the targeted well in the multi-well horizontal pad.

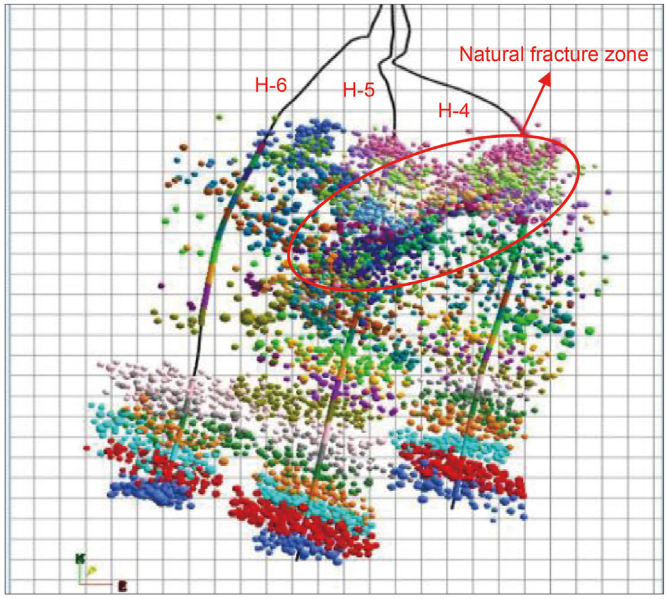

Fig. 26. Microseismic events of wells H-4, H-5, and H-6 in Changning area.

targeted well occurring later. Moreover, when the impact of the offsetting well on the targeted well occurs, the bottom hole pressure and pressure derivative curves of the targeted well suddenly surge.

5.2.9. *Effect of varying water saturation on the SRV region*

The significant retention of fracturing fluid in the reservoir during horizontal well fracturing operations leads to reservoir damage, which subsequently affects the flow of natural gas within the reservoir. Analyzing the transient behavior of the targeted well for different water saturation levels in the SRV region, ranging from 0 to 40%, as shown in Fig. 24, reveals that the varying water saturation in the SRV region primarily impacts the early production stage. Higher water saturation increases the resistance to the flow of natural gas in the reservoir, resulting in higher pressure and pressure derivative curves for the targeted well. However, as the pressure wave propagates to the boundary of the SRV region, the influence of water saturation on the transient behavior at the

Table 3
Input parameters of the case study from the Changning area.

Group	Item	Value	Unit
Basic parameters	Initial reservoir pressure	35	MPa
	Reservoir thickness	40	m
	Rock compressibility	4.35×10^{-4}	MPa^{-1}
	Porosity	0.03	–
H-4 well	Fracture width	0.001	m
	Fracture porosity	0.5	–
	Fracture number	23	–
	Well length	1500	m
H-5 well	Fracture width	0.001	m
	Fracture porosity	0.5	–
	Fracture number	23	–
	Well length	1800	m
H-6 well	Fracture width	0.001	m
	Fracture porosity	0.5	–
	Fracture number	22	–
	Well length	1510	m
Fluid	Viscosity	0.25	mPa·s
	Compressibility	0.018	MPa^{-1}

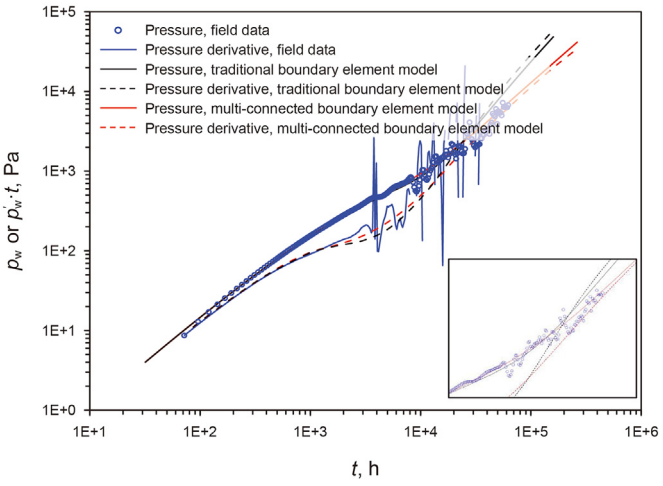

Fig. 28. Case study of the shale gas reservoir in the Changning area: Typical curve matching results for well H-5.

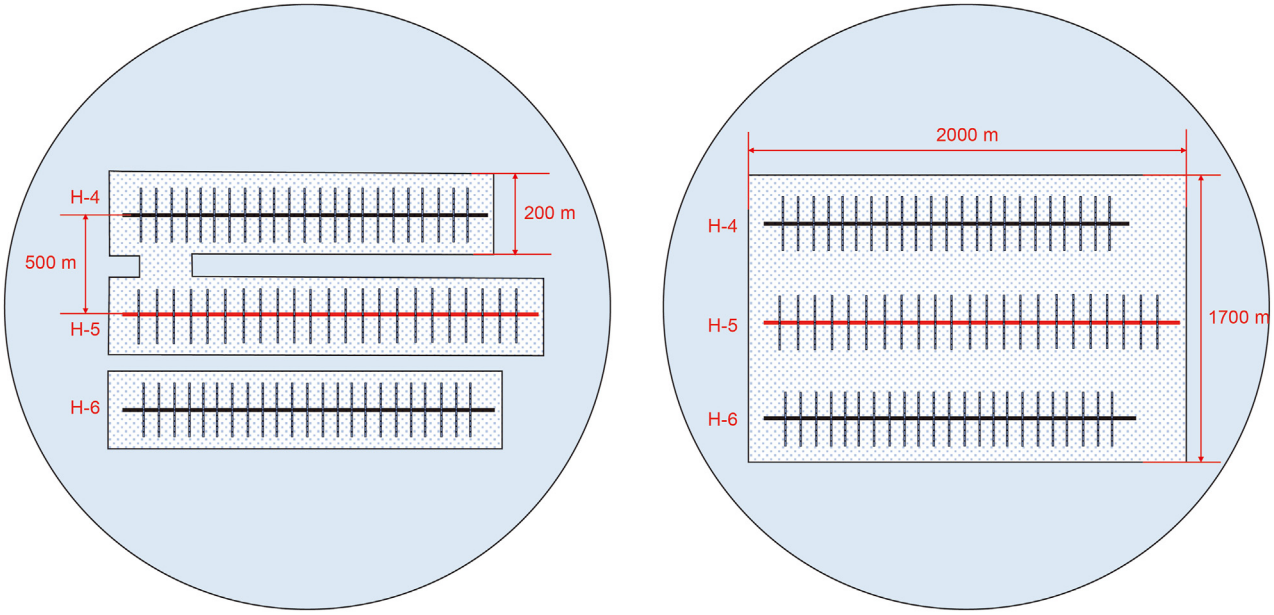

(a) Multi-connected boundary element model **(b)** Traditional boundary element model

Fig. 27. Model schematic diagram.

bottom of the targeted well gradually diminishes.

5.2.10. Effect of different diffusion coefficients

The Knudsen diffusion coefficient primarily affects the process of natural gas migration from matrix pores to natural fractures in a dual-porosity medium. As shown in Fig. 25, a smaller diffusion coefficient delays the occurrence of matrix-to-fracture gas migration, causing the concavity in the pressure derivative curve of the target well to shift to the right. The magnitude of the concavity is also influenced by the diffusion coefficient. A larger diffusion coefficient results in a more pronounced concavity in the pressure derivative curve, while a smaller coefficient leads to a less pronounced concavity.

6. Field application

The study focuses on the Longmaxi Formation shale gas reservoir in the Changning area, located in the Changning Block, Yibin, Sichuan. The structural position is at the junction of the Sichuan Basin and the Yunnan-Guizhou Plateau. In this study case, three wells were drilled in September 2014 and monitored for pressure and production rate from January 2015 to September 2023. The well lengths of wells H-4, H-5, and H-6 are 1500, 1800, and 1510 m long, respectively, with well spacings of approximately 500 m. Microseismic events for this area (Fig. 26) indicate that wells H-5 and H-4 are partially connected through a natural fracture zone. Other parameters for this area are shown in Table 3.

Field monitoring data indicate a significant upward trend in the pressure curve of well H-5 during the mid to late production stages,

Table 4
Evaluation results of the case study from the Changning area.

Group	Item	Value	Unit
Basic parameters	Well spacing	480	m
	Matrix permeability	6.5×10^{-4}	mD
	Nature-fracture permeability	1.8	mD
H-4 well	Fracture half length	75	m
	Fracture conductivity	90	mD·m
	Fracture dip angle	90	°
H-5 well	Fracture half length	82	m
	Fracture conductivity	85	mD·m
	Fracture dip angle	90	°
	Skin factor	0	–
	Wellbore storage coefficient	35	m^3/MPa
H-6 well	Fracture half length	75	m
	Fracture conductivity	90	mD·m
	Fracture dip angle	90	°

suggesting substantial interwell interference. To demonstrate the advantages of the model presented in this paper, we established two models (Fig. 27) to fit the actual curve of well H-5. The fitting results are shown in Fig. 28. It can be observed that the multi-connected boundary element model enters the transition flow stage from the SRV region to the uSRV region earlier, and the interwell interference experienced by the multi-connected boundary element model is less than that of the traditional boundary element model. The fitting results indicate that, in this case, the traditional boundary element model overestimates the degree of interwell interference, whereas the multi-connected boundary element model handles this situation well. The parameters obtained from the evaluation for the three wells are shown in Table 4.

7. Conclusions

Based on the multi-connected boundary element method and considering the adsorption-desorption effect of natural gas in shale reservoirs and the impact of bound water, we categorized the connectivity of the complex SRV region in multi-well horizontal pads into three scenarios and established respective models. We analyzed the effects of SRV region connectivity, reservoir properties, scale of SRV region, bound water saturation, as well as the production time of the target and offset wells on the transient pressure behavior of multi-well horizontal pads. The main conclusions are as follows.

(1) When the SRV regions of the targeted well and the offsetting well are not connected, the stage of transitional flow from the SRV region to the uSRV region arrives earlier than the interwell interference flow stage for the targeted well. This is one of the distinctions from other models.
(2) When the production rates of the offsetting well and the targeted well differ, the connectivity of the SRV regions significantly affects the production of the targeted well. Specifically, when the production rate of the offsetting well exceeds that of the targeted well, the connectivity of the SRV regions leads to an increase in the pressure and pressure derivative curves of the targeted well. Conversely, when the production rate of the offsetting well is lower than that of the targeted well, the connectivity of the SRV regions results in decreases in the pressure and pressure derivative curves of the targeted well. However, when the SRV regions are not connected, the impact on the targeted well is limited regardless of the production rate of the offsetting well.
(3) When the SRV regions of the offsetting well and the targeted well are not connected, the size and properties of the SRV regions around the offsetting well have a limited impact on the production of the targeted well, mainly observed in the late stage of production. In contrast, the size and properties of the SRV regions around the targeted well have a significant impact on the production of the targeted well, primarily observed in the pre-production stage.
(4) The different production start times of offsetting well and well spacing directly affect the onset of the interwell interference flow stage in the targeted well. The later the offsetting well starts production and the larger the well spacing, the later the targeted well enters the interwell interference flow stage.

Since this model requires detailed characterization of the SRV region in the horizontal well platform, it relies on field microseismic monitoring and horizontal well fracturing design during the modeling process. Therefore, the accuracy of parameter inversion is limited by the data provided from the field. Additionally, this model cannot account for fracture hits, which presents certain limitations in practical applications. To address these issues, the next research goal is to consider fracture hits between wells. Additionally, establishing a scientific workflow to achieve synergy between field operations and laboratory experiments is also a priority.

CRediT authorship contribution statement

Yu-Long Zhao: Writing – review & editing, Writing – original draft, Visualization, Validation, Supervision, Software, Resources, Project administration, Methodology, Investigation, Funding acquisition. **Hao-Yan Feng:** Data curation, Formal analysis, Investigation, Methodology, Software, Validation, Writing – original draft. **Cheng-Zhong Bu:** Resources, Funding acquisition. **Li-Sha Zhou:** Resources, Funding acquisition. **Jian-Fa Wu:** Resources, Funding acquisition. **Lie-Hui Zhang:** Resources, Funding acquisition. **Ying-Fang Zhou:** Writing – review & editing, Writing – original draft.

Declaration of competing interest

The authors declare that they have no known competing financial interests or personal relationships that could have appeared to influence the work reported in this paper.

Acknowledgments

This research is supported by the National Science Fund for Excellent Young Scholars (No. 52222402), State Key Program of National Natural Science Foundation of China (No. U23A2022), State Key Program of National Natural Science Foundation of China (No. 52234003), Sichuan Science and Technology Program (No. 2022JDJQ0009), National Natural Science Foundation of China (No. 52074235), Science and Technology Cooperation Project of the CNPC-SWPU Innovation Alliance (Nos. 2020CX020202 and 2020CX030202), Shale Gas industry Development Institute of Sichuan Province and 111 Project (No. D18016), China Postdoctoral Science Foundation (No. 2022M722637), and the Science Foundation of Sichuan Province (No. 2022NSFSC0186).

References

Afsharpoor, A., Javadpour, F., 2018. Pore connectivity between organic and inorganic matter in shale: network modeling of mercury capillary pressure. Transport Porous Media 125 (3), 503–519. https://doi.org/10.1007/s11242-018-1132-0.

Al-Shami, T.M., Jufar, S.R., Kumar, S., et al., 2023. A comprehensive review of interwell interference in shale reservoirs. Earth Sci. Rev. 237, 104327. https://doi.org/10.1016/j.earscirev.2023.104327.

Asadi, M.B., Dejam, M., Zendehboudi, S., 2020. Semi-analytical solution for productivity evaluation of a multi-fractured horizontal well in a bounded dual-porosity reservoir. J. Hydrol. 581, 124288. https://doi.org/10.1016/j.jhydrol.2019.124288.

Chen, X.X., Liu, P.C., 2023. Pressure transient analysis of a horizontal well intercepted by multiple hydraulic fractures in heterogeneous reservoir with multiple connected regions using boundary element method. J. Hydrol. 616, 128826. https://doi.org/10.1016/j.jhydrol.2022.128826.

Chen, Z.M., Zhou, B., Zhang, S.Q., et al., 2023. Pressure transient behaviors for horizontal wells with well interferences, complex fractures and two-phase flow. Geoenergy Science and Engineering 227, 211845. https://doi.org/10.1016/j.geoen.2023.211845.

Chu, H.Y., Chen, Z.M., Liao, X.W., et al., 2022a. Transient behavior modeling of a multi-well horizontal pad in a reservoir with irregular boundary using boundary element method. J. Petrol. Sci. Eng. 209, 109852. https://doi.org/10.1016/j.petrol.2021.109852.

Chu, H.Y., Ma, T.B., Gao, Y.B., et al., 2022b. A composite model based on semi-analytical method for multi-well horizontal pad with stimulated reservoir volume. J. Petrol. Sci. Eng. 217, 110910. https://doi.org/10.1016/j.petrol.2022.110910.

Cui, Y.Z., Jiang, R.Z., Wang, Q., et al., 2021. Production performance analysis of multi-fractured horizontal well in shale gas reservoir considering space variable and stress-sensitive fractures. J. Petrol. Sci. Eng. 207, 109171. https://doi.org/10.1016/j.petrol.2021.109171.

Fu, Y.H., Jiang, Y.Q., Dong, D.Z., et al., 2021. Microscopic pore-fracture configuration and gas-filled mechanism of shale reservoirs in the western Chongqing area, Sichuan Basin, China. Petrol. Explor. Dev. 48 (5), 1063–1076. https://doi.org/10.1016/S1876-3804(21)60091-5.

Fu, H.Y., Liu, H., Hu, X.H., et al., 2023. Horizontal well interference performance and water injection huff and puff effect on well groups with complex fracture networks: a numerical study. Comput. Model. Eng. Sci. 137 (3), 2285–2309. https://doi.org/10.32604/cmes.2023.027996.

Gao, D.P., Liu, Y.W., Wang, D.G., et al., 2019. Numerical analysis of transient pressure behaviors with shale gas MFHWs interference. Energies 12 (2), 262. https://doi.org/10.3390/en12020262.

Garcez, J., Ayala, L.F., 2022. Green's function-based type curves for multi-fractured horizontal gas wells in unconventional reservoirs. Fuel 320, 123713. https://doi.org/10.1016/j.fuel.2022.123713.

Gringarten, A.C., Ramey, H.J., 1973. The use of source and green's functions in solving unsteady-flow problems in reservoirs. SPE J. 13 (5), 285–296. https://doi.org/10.2118/3818-PA.

Gringarten, A.C., Ramey, H.J., 1974. Unsteady-state pressure distributions created by a well with a single infinite-conductivity vertical fracture. SPE J. 14 (4), 347–360. https://doi.org/10.2118/4051-PA.

Guo, J.J., Wang, H.Y., Zhang, L.H., 2016. Transient pressure and production dynamics of multi-stage fractured horizontal wells in shale gas reservoirs with stimulated reservoir volume. J. Nat. Gas Sci. Eng. 35, 425–443. https://doi.org/10.1016/j.jngse.2016.08.074.

Guo, T.L., Kou, Z.H., Zhao, Y.L., et al., 2023. Role of gas multiple transport mechanisms and fracture network heterogeneity on the performance of hydraulic fractured multi-well pad in unconventional reservoirs. Fuel 342, 127808. https://doi.org/10.1016/j.fuel.2023.127808.

Han, H., Pang, P., Li, Z.L., et al., 2019. Controls of organic and inorganic compositions on pore structure of lacustrine shales of Chang 7 member from Triassic Yanchang Formation in the Ordos Basin, China. Mar. Petrol. Geol. 100, 270–284. https://doi.org/10.1016/j.marpetgeo.2018.10.038.

He, Y.W., Cheng, S.Q., Rui, Z.H., et al., 2018. An improved rate-transient analysis model of multi-fractured horizontal wells with non-uniform hydraulic fracture properties. Energies 11 (2), 393. https://doi.org/10.3390/en11020393.

He, Y.W., He, Z.Y., Tang, Y., et al., 2023. Interwell fracturing interference evaluation in shale gas reservoirs. Geoenergy Science and Engineering 231, 212337. https://doi.org/10.1016/j.geoen.2023.212337.

Hou, B., Zhang, Q.X., Liu, X., et al., 2022. Integration analysis of 3D fractures network reconstruction and frac hits response in shale wells. Energy 260, 124906. https://doi.org/10.1016/j.energy.2022.124906.

Jia, P., Cheng, L.S., Clarkson, C., et al., 2017a. A Laplace-domain hybrid model for representing flow behavior of multifractured horizontal wells communicating through secondary fractures in unconventional reservoirs. SPE J. 22 (6), 1856–1876. https://doi.org/10.2118/186109-PA.

Jia, P., Cheng, L.S., Huang, S.J., et al., 2017b. A comprehensive model combining Laplace-transform finite-difference and boundary-element method for the flow behavior of a two-zone system with discrete fracture network. J. Hydrol. 551, 453–463. https://doi.org/10.1016/j.jhydrol.2017.06.022.

Kumar, A., Seth, P., Shrivastava, K., et al., 2020. Integrated analysis of tracer and pressure-interference tests to identify well interference. SPE J. 25 (4), 1623–1635. https://doi.org/10.2118/201233-PA.

Li, B., 2022. Modeling of shale gas transport in multi-scale complex fracture networks considering fracture hits. Transport Porous Media 149 (1), 71–86. https://doi.org/10.1007/s11242-022-01835-y.

Li, J., Chen, Z.X., Wu, K.L., et al., 2018. Effect of water saturation on gas slippage in tight rocks. Fuel 225, 519–532. https://doi.org/10.1016/j.fuel.2018.03.186.

Liang, Y.B., Cheng, Y.F., Han, Z.Y., et al., 2024. Numerical simulation analysis on production evolution laws in shale reservoirs considering a horizontal well interwell interference effect. Energy Fuels 38, 4076–4090. https://doi.org/10.1021/acs.energyfuels.3c04951.

Manchanda, R., Sharma, M.M., Holzhauser, S., 2014. Time-dependent fracture-interference effects in pad wells. SPE Prod. Oper. 29 (4), 274–287. https://doi.org/10.2118/164534-PA.

Marongiu-Porcu, M., Lee, D., Shan, D., et al., 2016. Advanced modeling of interwell-fracturing interference: an eagle ford shale-oil study. SPE J. 21 (5), 1567–1582. https://doi.org/10.2118/174902-PA.

Mayerhofer, M.J., Lolon, E.P., Warpinski, N.R., et al., 2010. What is stimulated reservoir volume? SPE Prod. Oper. 25 (1), 89–98. https://doi.org/10.2118/119890-PA.

Molina, O.M., 2019. Analytical model to estimate the fraction of frac hits in multi-well pads. In: SPE/AAPG/SEG Unconventional Resources Technology Conference. https://doi.org/10.15530/urtec-2019-238.

Molina, O.M., Zeidouni, M., 2017a. Analytical approach to determine the degree of interference between multi-fractured horizontal wells. In: SPE Europec Featured at 79th EAGE Conference and Exhibition. https://doi.org/10.2118/185765-MS.

Molina, O.M., Zeidouni, M., 2017b. Analytical model to estimate the fraction of fracture hits in a multi-well pad. In: SPE Liquids-Rich Basins Conference. https://doi.org/10.2118/187501-MS.

Qin, J.Z., Zhong, Q.H., Tang, Y., et al., 2023. Well interference evaluation considering complex fracture networks through pressure and rate transient analysis in unconventional reservoirs. Petrol. Sci. 20, 337–349. https://doi.org/10.1016/j.petsci.2022.09.029.

Raterman, K., Liu, Y.S., Roy, B., et al., 2020. Analysis of a multi-well eagle ford pilot. In: SPE/AAPG/SEG Unconventional Resources Technology Conference. https://doi.org/10.15530/urtec-2020-2570.

Siddiqui, S., Kumar, A., 2016. Well interference effects for multiwell configurations in unconventional reservoirs. In: Abu Dhabi International Petroleum Exhibition & Conference. https://doi.org/10.2118/183064-MS.

Tan, Y.L., Zhang, S.H., Tang, S.H., et al., 2021. Impact of water saturation on gas permeability in shale: experimental and modelling. J. Nat. Gas Sci. Eng. 95, 104062. https://doi.org/10.1016/j.jngse.2021.104062.

Wang, B., Zhang, Q.S., Yao, S.S., et al., 2022. A semi-analytical mathematical model for the pressure transient analysis of multiple fractured horizontal well with secondary fractures. J. Petrol. Sci. Eng. 208, 109444. https://doi.org/10.1016/j.petrol.2021.109444.

Wang, J.L., Jia, A.L., Wei, Y.S., et al., 2018. Laplace-domain multiwell convolution for simulating pressure interference response of multiple fractured horizontal wells by use of modified Stehfest algorithm. J. Petrol. Sci. Eng. 161, 231–247. https://doi.org/10.1016/j.petrol.2017.11.074.

Wu, J.F., Zhang, J., Chang, C., et al., 2020. A model for a multistage fractured horizontal well with rectangular SRV in a shale gas reservoir. Geofluids 2020, 8845250. https://doi.org/10.1155/2020/8845250.

Wu, M.L., Ding, M.C., Yao, J., et al., 2018. Pressure transient analysis of multiple fractured horizontal well in composite shale gas reservoirs by boundary element method. J. Petrol. Sci. Eng. 162, 84–161. https://doi.org/10.1016/j.petrol.2017.12.024.

Xu, J.L., Xu, Y.J., Wang, Y., et al., 2023. Multi-well pressure interference and gas channeling control in w shale gas reservoir based on numerical simulation. Energies 16 (1), 261. https://doi.org/10.3390/en16010261.

Zhang, D.L., Zhang, L.H., Guo, J.J., et al., 2015. Research on the production performance of multistage fractured horizontal well in shale gas reservoir. J. Nat. Gas Sci. Eng. 26, 279–289. https://doi.org/10.1016/j.jngse.2015.06.032.

Zhang, J.Y., Feng, Q.H., Zhang, X.M., et al., 2020. Multi-fractured horizontal well for improved coalbed methane production in eastern Ordos basin, China: field observations and numerical simulations. J. Petrol. Sci. Eng. 194, 107488. https://doi.org/10.1016/j.petrol.2020.107488.

Zhang, L.H., Gao, J., Hu, S.Y., et al., 2016. Five-region flow model for MFHWs in dual porous shale gas reservoirs. J. Nat. Gas Sci. Eng. 33, 1316–1323. https://doi.org/10.1016/j.jngse.2016.05.063.

Zhang, L.H., Shan, B.C., Zhao, Y.L., et al., 2019. Review of micro seepage mechanisms in shale gas reservoirs. Int. J. Heat Mass Tran. 139, 144–179. https://doi.org/10.1016/j.ijheatmasstransfer.2019.04.141.

Zhao, Y.L., Zhang, L.H., Luo, J.X., et al., 2014. Performance of fractured horizontal well with stimulated reservoir volume in unconventional gas reservoir. J. Hydrol. 512, 447–456. https://doi.org/10.1016/j.jhydrol.2014.03.026.

Zhao, Y.L., Shan, B.C., Zhang, L.H., et al., 2016. Seepage flow behaviors of multi-stage fractured horizontal wells in arbitrary shaped shale gas reservoirs. J. Geophys. Eng. 13 (5), 674–690. https://doi.org/10.1088/1742-2132/13/5/674.

Zhao, Y.L., Zhang, L.H., Shan, B.C., 2018. Mathematical model of fractured horizontal well in shale gas reservoir with rectangular stimulated reservoir volume. J. Nat. Gas Sci. Eng. 59, 67–79. https://doi.org/10.1016/j.jngse.2018.08.018.